Tailoring Sound and Vibrations with Acoustic Metamaterials

Mourad Oudich

Mémoire présenté en vue de l'obtention du diplôme d'Habilitation à Diriger des Recherches (HDR)

2 Octobre 2025

Présenté par

Mourad Oudich

Métamatériaux acoustiques pour le contrôle du son et des vibrations

Jury,

Rapporteur	Aloyse Degiron	Directeur de Recherche CNRS Laboratoire Matériaux et Phénomènes Quantiques, CNRS, Université Paris Cité
Rapporteur	Abdelkrim Talbi	Professeur des Universités Institut d'Electronique de Microélectronique et de Nanotechnologie, CNRS, Centrale Lille, Université de Lille, Université Polytechnique Hauts-de-France
Rapporteur	Vincent Tournat	Directeur de Recherche CNRS Laboratoire d'Acoustique de l'Université du Mans, CNRS, Institut d'Acoustique - Graduate School (IA-GS), Le Mans Université
Examinatrice	Thérèse Leblois	Professeure des Universités Institut FEMTO-ST, CNRS, Université de Franche-Comté
Examinateur	Nico F. Declercq	Professeur des Universités Georgia Institute of Technology
Examinateur (Parrain)	Badreddine Assouar	Directeur de Recherche CNRS Institut Jean Lamour, CNRS, Université de Lorraine.
Invité	Jean-François Ganghoffer	Professeur des Universités Laboratoire d'Étude des Microstructures et de Mécanique des Matériaux, CNRS, Université de Lorraine.

Institut Jean Lamour
Centre National de la Recherche Scientifique
Département Nanomatériaux, Electronique et Vivant
Equipe Métamatériaux et Phononique (407)

Université de Lorraine
Pôle matière matériaux métallurgie mécanique
Collégium Sciences et Technologies
Faculté des Sciences et Technologies

Table of contents

Remerciements

Je tiens à exprimer ma gratitude à Badreddine Assouar, mon ancien directeur de thèse, actuellement responsable de notre équipe Métamatériaux et Phononique, pour son accompagnement constant, sa confiance et son soutien tout au long de mon parcours.

Un grand merci à Yun Jing pour son accueil et soutien permanent durant mon détachement à North Carolina State University puis à Penn State University, une expérience d'une grande importance dans ma carrière.

Je remercie également Bahram Djafari-Rouhani et Yan Pennec, mes encadrants de postdoctorat à l'IEMN pour l'expérience inédite au sein de leur équipe.

Un immense merci à tou(te)s les doctorant(e)s que j'ai eu le plaisir de co-encadrer, ainsi qu'aux doctorant(e)s et post-doctorant(e)s avec qui j'ai collaboré au fil des années. Travailler à leurs côtés a été une source d'enrichissement continu.

Je suis également profondément reconnaissant à tous mes collaborateurs(trices), en France et à l'international, pour la richesse des échanges scientifiques et humains qui ont marqué notre travail commun.

Enfin, il n'y a pas de mots pour exprimer ma profonde gratitude à ma famille, dont le soutien indéfectible, la patience et l'amour ont été essentiels à chaque étape de ce parcours.

Merci à toutes et à tous, du fond du cœur.

General introduction

As a *Maître de Conférences* (Associate professor) at the University of Lorraine and the *Institut Jean Lamour* (CNRS), I specialize in wave physics, computational acoustics, and elastodynamics. My research primarily focuses on the structural design of phononic crystals and acoustic metamaterials to realize advanced wave control functionalities with strong potential for real-world applications. These include sound and vibration mitigation, wireless ultrasound-based energy and data transfer, energy harvesting, underwater sound absorption, ultra-sensitive microsensing, and optomechanics. In parallel, I explore how condensed matter physics phenomena can be emulated in acoustics and elastodynamics, investigating areas such as topological phononics, space-time phononic crystals, acoustic analogs of twisted bilayer superlattices, and topological pumping in the gigahertz regime. My long-standing fascination with phononic crystals and elastic metamaterials has recently led to the publication of a review article in *Advanced Functional Materials* and a perspective piece in *Nature Materials*.

Over the past twelve years, I have led and contributed to several collaborative research projects, co-supervised four PhD students, and worked closely with outstanding students, postdocs, and researchers worldwide.

This manuscript highlights several key projects I have conducted or been heavily involved in over the last 12 years:

- Chapter 1 offers a review of phononic crystals and metamaterials, highlighting their importance in shaping mechanical wave propagation and enabling new functionalities. It focuses on elastic wave propagation in solids, emphasizing phononic bandgaps, their underlying physical mechanisms, and various structural designs tailored for specific wave manipulation.
- Chapter 2 presents our research on planar metamaterials, referred to as acoustic metasurfaces, designed to achieve either broadband sound absorption or enhanced acoustic wave transmission, with direct applications in energy harvesting and wireless acoustic power/data transfer.
- Chapter 3 highlights our recent efforts to embed phononic crystals and metamaterials into microsystems, particularly surface acoustic wave (SAW) devices. The chapter demonstrates how engineering these phononic structures can produce high-Q elastic modes that are efficiently excited by SAWs, and leveraged to enhance micro/nano-particle detection sensitivity.
- Chapter 4 explores the emerging field of non-reciprocal acoustics using active, artificially modulated acoustic platforms known as space-time phononic crystals. We analyze their dispersive and nonreciprocal properties and demonstrate experimentally how compact systems can be designed for unidirectional acoustic wave propagation.
- The final chapter (Chapter 5) outlines the future directions of my research over the next five years. This includes the development of Moiré metamaterials, in the framework of my project as a Junior Fellow of the *Institut Universitaire de France* (IUF).

Chapter 1: Elastodynamic Metamaterials

In this chapter, we summarize the road for the establishment of phononic crystals and elastic metamaterials and their importance in term of wave physics and device engineering while presenting some applications, spanning from Hz to GHz frequency regimes. We will mainly focus on elastic waves, i.e. mechanical waves propagation in solid elastic medias, and the underlaying physics elastic bandgaps. We also present illustrative examples of structural designs tailored to achieve specific wave functionalities towards real-world applications.

1.1 Phononic bandgaps in elastic media

In solid-state physics, a bandgap (BG) is an energy range in which no electronic states can exist. This concept has been extended to classical waves (electromagnetic and acoustic waves), leading to the development of photonic and phononic crystals. These artificial crystals also exhibit an analog BGs defined as frequency (or wavelength) intervals where wave propagation is forbidden. In the context of elastic waves, such BGs arise from periodic spatial variations in mechanical properties such as stiffness and density. This principle drives the development of phononic crystals (PnC) and, subsequently, elastic metamaterials, which have unlocked unprecedented wave control capabilities for diverse applications. Early studies demonstrated that the opening of the BG was attributed to the Bragg scattering mechanism caused by the periodicity of the lattice. Later on, another type of BG was shown to originate fom strong localized elastic resonances within the PnC which was labeled as locally resonant PnC (LRPC).

1.1.1 Bragg bandgaps

Early studies on PnCs focused on BGs generated by the scattering of elastic waves due to the periodic architecture of the PnC[1–4]. These structures were typically designed using periodic layers for 1D wave propagation[1], or by embedding voids or solid inclusions within a host medium in 2D configurations[2–4]. A strong contrast in elastic properties between the inclusions and the surrounding matrix was essential for opening a BG (see **Fig. 1.1(a)**). The underlying mechanism responsible for the creation of such BGs was identified as Bragg scattering— wave interference phenomenon resulting from interactions with successive rows of periodic inclusions. Bragg-type BGs emerge at frequencies where the wavelength is comparable to the lattice periodicity, specifically when the wavelength is approximately twice the lattice periodicity. Wave dispersion in PnCs is analyzed through the computation of band structures, analogous to electronic band structures, where frequencies (instead of energy levels) of the propagating modes are displayed as a function of the wavevector within the Brillouin zone of the lattice (see lower panel of **Fig. 1.1(a)**).

1.1.2 Local resonance bandgaps

BGs can also arise from strong mechanical resonances, as first shown by Liu *et al.*[5]. Their structure features a three-dimensional (3D) lattice of spherical resonators, each composed of a heavy lead core coated with soft silicone, embedded in an epoxy matrix (upper panel of **Fig. 1.1(b)**). These resonators act as spring-mass systems with low stiffness and high mass, leading to localized resonance modes at very low frequencies. The BG forms through coupling between these localized modes and the bulk modes of the structure. In the band structure, the resonances appear as flat bands away from the Γ point, indicating zero group velocity and defining the lower edge of the BG (lower panel of **Fig. 1.1(b)**). Unlike Bragg BGs, locally resonant (LR) BGs depend only on the resonator's geometry and material properties, not on periodicity or symmetry. This allows tuning to deep subwavelength regimes, where wavelengths are much larger than the lattice periodicity. LR BGs have thus enabled compact structure designs for low-frequency wave attenuation and wave control.

Due to their deep subwavelength nature, LRPCs were analyzed using homogenization methods, revealing unusual dynamic behavior. It was shown that at resonance frequencies where the wavelength far exceeds the lattice spacing, the structure exhibits negative and even divergent effective mass density within the LR BG[5]. This discovery became a cornerstone in the development of acoustic and elastic metamaterials, redefining mechanical wave control.

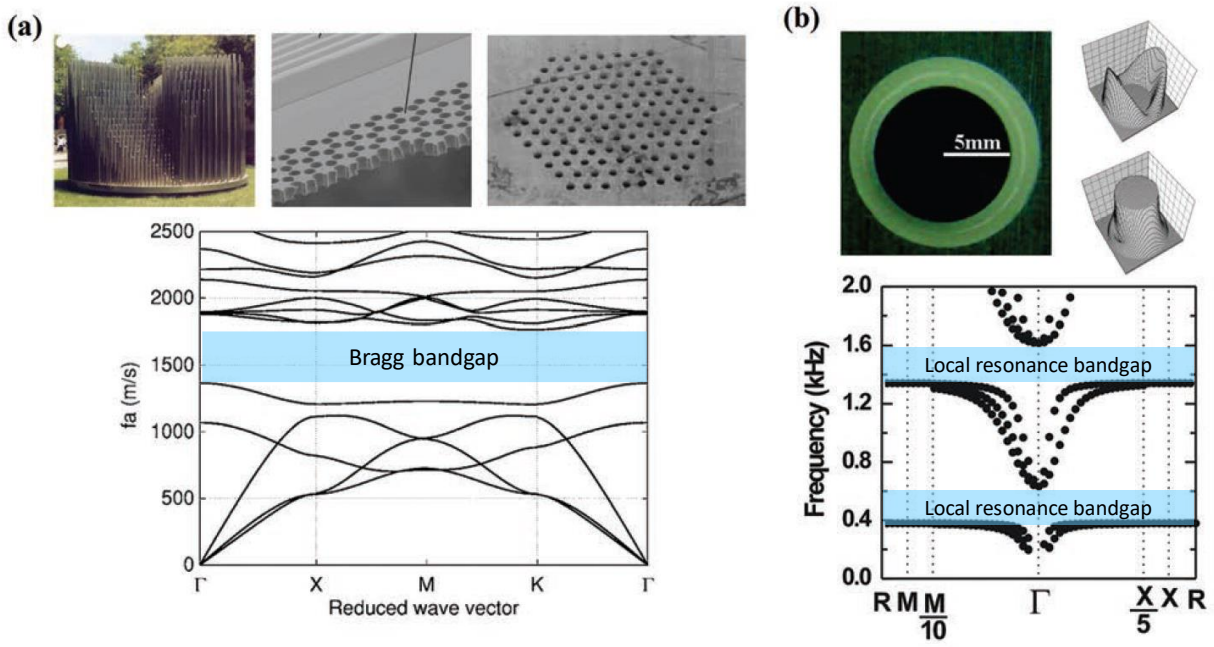

Fig 1.1. Phononic crystals and locally resonant metamaterials. (a) Examples of PnCs. (Top from left to right) 2D lattice of rods in air[6], Micro-holes in a plate[7], and Holes in a marble quarry[8]. (Bottom panel) Band structure of a PnC plate with a Bragg BG[9]. (b) Unit cell of a 3D lattice of a LR PnC (upper panel), and its associated band structure showing two local resonance BGs[5] (bottom panel).

1.2 Structural design of PnCs and metamaterials for bandgap engineering: contemporary avenues

Early research on elastic BGs established the foundation for understanding their underlying physical mechanisms and their dependence on the structural design of PnCs and metamaterials. These insights enabled effective control over mechanical wave propagation and opened new avenues for exploring wave physics and engineering these artificial materials for practical applications. Central to this field is the ability to create and precisely tune elastic BGs, both in width and spectral position, which has led to the emergence of BG

engineering. This area has become essential for a wide range of advanced acoustic platforms and wave functionalities, including optomechanical systems, elastic topological insulators for robust waveguiding and confinement, acoustic energy harvesting, PnC-based sensing, active and reconfigurable metamaterials, and inverse design approaches for tailored BG properties.

1.2.1 Optomechanical crystals

Phononic BG engineering has become essential in the context of optomechanical device design as it has boosted their mechanical performance by increasing the phonon lifetime for enhanced optomechanical interactions. In the last two decades, we have witnessed a rise in interests toward both photonic and phononic crystals, leading to the birth of a combination of the two crystals, called phoxonic crystal (PxC) (the "x" stands for both "t" and "n") which is a dual photonic and phononic crystal that exhibits simultaneously BGs for optical and mechanical waves[10–15]. With this dual BGs, a carefully engineered structural defect in the PxC allows it to host both optical and elastic cavity modes within their respective BGs, which results in strong confinement of electromagnetic and mechanical energy within the defect region. This leads to enhanced optomechanical interaction within the cavity. An example is illustrated in **Fig. 1.2(a)**: a one-dimensional silicon-based PxC nanobeam designed with a tapered cavity formed by gradually varying the periodicity at its center (**Fig.1.2(b)**) to enable high quality factor optical and mechanical modes trapping[16,17] (**Fig.1.2(c)**). Phononic BGs have become essential for high performance optomechanics, as phononic shields are used to suppress the mechanical losses created from coupling between the mechanical modes due to symmetry breaking caused by fabrication imperfections at the nanoscale[14,15,18]. Further, these BGs were tailored to achieve cavity-optomechanical circuits that could potentially be used for performing controlled coherent signal processing[19]. Thanks to the remarkable sensitivity of optomechanical resonators for detecting single biological species[20] and individual molecules[21], PxCs have demonstrated exceptional capabilities in locating microparticles[22]. Moreover, another promising application of PxCs is the generation of quantum entanglement between mechanical states[23], which could open new avenues for the development of silicon-based quantum networks.

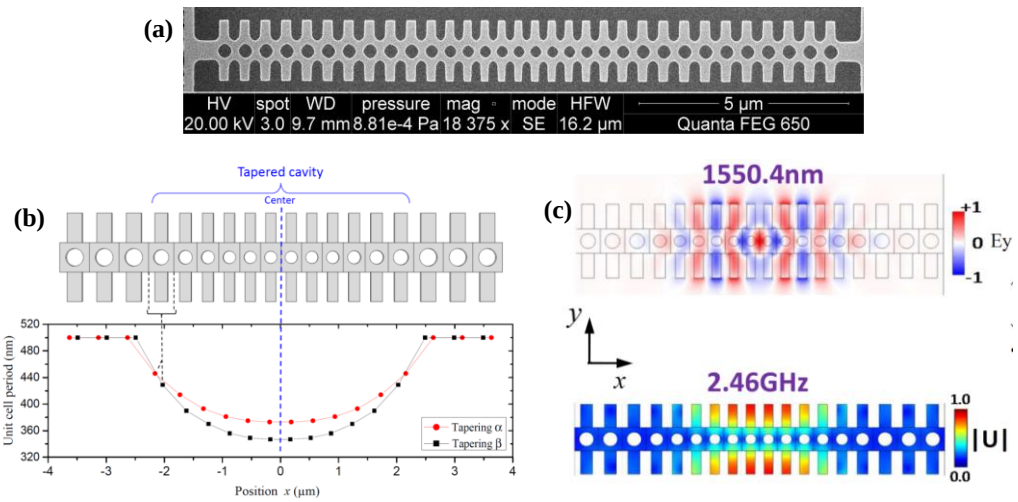

Fig .1.2. (a) SEM Image of a fabricated PxC with a tapered cavity. (b) Schematic view of the tapered cavity created inside the phoxonic nanobeam by gradually changing the unit cells period in space. The red and black connected dots show two different tapering profiles for two tapered cavities. (c) Wavefields of the trapped cavity for the optical mode at 1550.4 nm and the phononic mode at 2.46 GHz[16,17].

1.2.2 Topological elastodynamics

The Nobel-winning discovery of topological phases by Thouless, Haldane, and Kosterlitz led to the rise of topological materials like topological insulators, known for symmetry-driven phase transitions and nontrivial features such as nonzero Chern numbers. Photonic and phononic crystals have become powerful platforms for exploring topological physics by emulating quantum phenomena in classical systems. Topological BGs are the cornerstone of topological physics and can emerge from mechanisms such as the quantum Hall (QH)[24–26], spin Hall (QSH) [27–29], and valley Hall (QVH) effects[30–33], enabling robust and unconventional wave control. This sparked demonstrating quantum-like mechanical phenomena at the mesoscopic and macroscopic scales using PnCs leading to unprecedented acoustic and elastic wave control such as topological interface, edge and corner states[34,35,31], Weyl points[36,37], and topological pumping[38].

Elastic topological insulators are engineered to generate pseudospins ±1/2 and artificial Kramers pairs, characterized by a Z2 topological invariant, hence called Z2 topological insulators. One design approach involves creating two Dirac cones in the band structure where breaking the lattice symmetry lifts the Dirac degeneracy, inducing an effective spin–orbit coupling, and enabling nontrivial interface states that support helical elastic edge waves[29]. Another strategy exploits modal hybridization[39,40] which creates a double Dirac point. When this degeneracy is lifted, distinct pseudospin states emerge, opening a topological BG (**Fig.1.3**). A simpler route, known as zone folding, brings two Dirac cones from the K point to Γ, facilitating the design of Z2 topological insulators in elastic plates[39–41] and surface acoustic wave (SAW) systems[42]. In addition, the QVH effect has been used to design elastic topological PnCs by breaking spatial inversion symmetry in honeycomb lattices. This lifts the Dirac degeneracy at the K point and gives rise to valley states with opposite ±1/2 pseudospins, which support robust valley-polarized edge modes. A key advantage of these topological edge waves is their robustness against defects, as demonstrated in several studies involving point, line, and arbitrary defects created by removing or deforming unit cells[26,27,31,34,39,42,43]. This robustness makes topological edge states particularly attractive for practical applications.

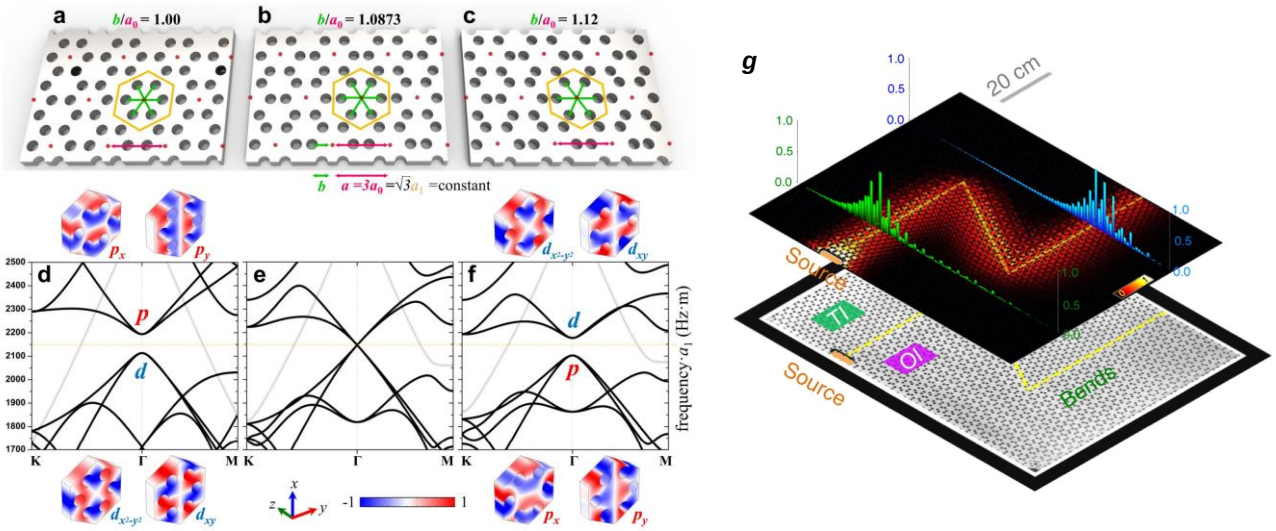

Fig. 1.3. Elastic band inversion with an overlapped BG in a PnC. (a)-(c): PnC plate composed of identical perforated holes. In in each unit-cell, as the yellow hexagons indicate, the length between the center of the six perforated holes and the center of the unit-cell, b, increases from (a) a_0, to (b) $1.0873a_0$, and (c) $1.12a_0$. (d) - (f): Band structures of the three PnC cases illustrating a band inversion with an overlapped BG. Two two-fold degenerate states, labeled p_x/p_y and d_{x2-y2}/d_{xy}, are separated by an elastic BG. When b increases to $1.0873a_0$, the BG closes and an accidental double Dirac cone with a four-fold degeneracy is formed. When b further increases to $1.12a_0$, the BG reappears along with two inverted two-fold degeneracies corresponding to d_{x2-y2}/d_{xy} and p_x/p_y. The insets surrounding the band diagrams are the elastic displacement distributions of the degenerate elastic eigenstates in the out-of-plane direction. (g) A Z-shaped bend waveguide with the elastic energy-density distributions for elastic waves at a frequency (110.0 kHz) within the BG. Green and blue bars are experimental measurements[39].

In classical wave systems, topological phenomena are often expressed through dimensional reduction, such as the emergence of 1D edge states in 2D lattices. Beyond the conventional bulk-edge (2D–1D) correspondence, 2D systems can also exhibit bulk-corner (2D–0D) correspondence, leading to localized 0D topological corner states—features that arise in systems with higher-order topology[44–46]. This intrinsic defect immunity has also inspired exploration of topological mechanical edge states in amorphous systems, including hyperuniform structures, quasicrystals, and even randomly distributed lattices. Several studies have assessed their robustness to structural defects, introduced via point, line, or arbitrary modifications such as the removal or deformation of unit cells.

1.2.3 Energy harvesting

Driven by the global demand for sustainable and renewable energy sources, acoustic energy harvesting (AEH) has gained significant attention, where the objective is to capture the energy carried by sound and vibrations and convert it into exploitable electrical power. Traditionally, this is achieved using a resonant cavity containing a vibrating elastic element coupled to a piezoelectric material, which transforms dynamic strain energy into electricity. Early AEH designs included Helmholtz resonators with vibrating membranes attached to piezoelectric rings[47], cantilevers[48], or arrays of piezoelectric plates placed within straight acoustic tubes[49,50]. With the advent of PnCs and acoustic metamaterials for advanced wave manipulation, these artificial materials have been further explored in the context of energy harvesting. PnCs can be engineered to confine wave energy efficiently by introducing a cavity defect within the periodic structure. When a BG is designed around a target frequency, a carefully tailored defect can support a localized cavity mode with strongly confined elastic energy. This concentrated energy can then be harvested using conventional piezoelectric elements.

A more comprehensive discussion of AEH using PnCs and metamaterials, along with our own contributions, including the design of a compact subwavelength metamaterial plate for efficient AEH, is presented in **Section 2.2** of ***Chapter 2***.

1.2.4 PnC and metamaterials for enhanced sensing

Numerous studies have investigated the potential of phononic BGs for sensing applications. The core mechanism relies on localized cavity modes confined within structural defects at frequencies lying inside the BG, which are highly sensitive to acoustic or elastic perturbations. Early work in this area employed PnCs with lattice constants and cavity dimensions on the order of a few centimeters, operating in the hundreds of

kHz to a few MHz range, to probe the properties of liquids. These initial designs featured liquid-filled cavities within the PnC to monitor changes in solution concentrations (e.g., 2-propanol, gasoline), as variations in concentration affect the wave velocity in the fluid medium[51–53]. Shifts in the resonance frequency of the defect modes were used to detect changes in the molar ratio of the solution, such as mixtures of propanol and water. More recently, metamaterial structures based on pillar arrays have been engineered and optimized for enhanced liquid sensing at the microscale, exploiting the interaction between the pillars and either Lamb waves[54] or SAW[55,56]. ***Chapter 3*** of this manuscript presents our recent studies[55,56] on the design strategies for PnC and metamaterials tailored for integration into SAW-based sensing platforms, aiming to improve their detection sensitivity and performance.

1.2.5 Ultra-light architected metamaterials for BG engineering

In the last decade, high interest was brought to the development of artificial materials that can simultaneously exhibit multiple functionalities, particularly combining low density with high mechanical strength. Such material are crucial for aeronautics, aerospace, and automotive sectors where durability and energy efficiency are of high importance. Nature offers inspiration in this regard, with examples such as wood[57], bones, exoskeletons, and spider silk[58] which all feature hierarchical structuration from micro- to macroscales to achieve exceptional mechanical performance at low densities. Inspired by these natural architectures, researchers have leveraged modern fabrication methods to reproduce their complex microstructures. In particular, additive manufacturing has unlocked the ability to fabricate architected materials with highly precise geometries across various hierarchical levels using single-phase architected metamaterials[59,60]. These materials demonstrate exceptional mechanical behaviors such as enhanced compressive recoverability[61], superelasticity[59,60], and the decoupling of mass density from stiffness[61].

This precise control over geometry and composition at the microscale also benefits mechanical wave manipulation. Using 3D printing, researchers have fabricated lightweight, single-phase architected lattices exhibiting broad BGs, mostly with centimeter-scale lattice constants leading to low-frequency BGs[62]. Other strategies introduced embedded or connected masses to induce LR BGs with wider bandwidths but at the expense of increased mass[63–65]. An innovative lightweight design employing single phase curved metallic beams without added mass was proposed to attain a wide ultrasonic BG[66]. The metamaterial was fabricated using electron beam melting, a powder-based additive manufacturing technique. Recently, we have advanced this approach by constructing a polymeric auxetic metamaterial composed of thin struts, with a isotoxal star-shape design in 3D[67] (**Fig. 1.4(a)**). This ultralight structure (density: 0.034 g.cm^{-3}, lattice constant of 2 cm) exhibited a remarkable 82.8% BG width between 2.3 and 5.55 kHz (**Fig. 1.4(b)-(d)**), linked to a combination of negative/divergent effective bulk modulus and near-zero positive mass density. This structure was produced using high-resolution projection micro-stereolithography.

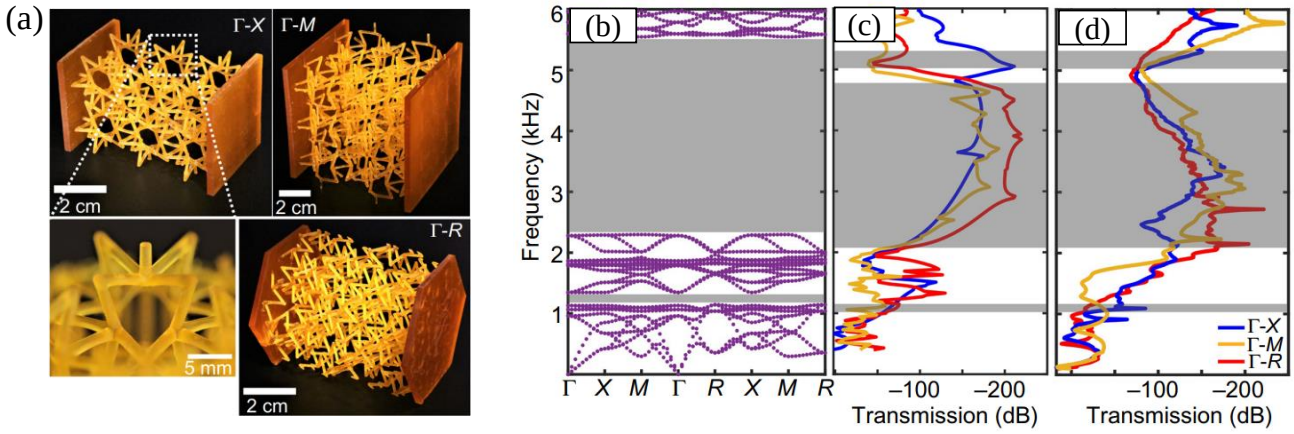

Fig. 1.4. (a) Photographs of the ultralight isotoxal star-based auxetic metamaterial samples, fabricated in the ΓX (top left), ΓM (top right), and ΓR (bottom right) directions, with the same unit-cell dimensions and with period, p = 2 cm. Bottom left panel shows a close-up optical image of the ΓX sample. (b) Elastic band structure of the auxetic lattice where the gray area highlights the wide BG. (c) Transmission simulations through the three samples. (d) Experimentally measured elastic wave transmission through the three samples.

However, achieving such performance in BG width requires not only precision in 3D printing but also a deep understanding of the mechanical properties of the base materials. Although additive manufacturing has advanced to accommodate a variety of substances, polymers remain the most common in architected lattices due to their versatility, yet their mechanical properties (e.g., stiffness and loss factor) vary with orientation, temperature, and frequency, complicating accurate dynamic modeling. This unpredictability challenges precise numerical predictions of metamaterials behavior. Nonetheless, newer additive manufacturing techniques now support printing with metals[59], ceramics[68], and even multiple materials simultaneously[69], offering promising though still underexplored avenues for more reliable low-dissipation elastic metamaterials.

1.2.6 Active elastodynamic metamaterials

While BGs in PnCs and elastic metamaterials enable a wide range of applications, they remain limited by fixed geometric and material properties set during fabrication. These constraints restrict BG width and frequency tunability. To overcome this, researchers have actively explored the incorporation of active elements into PnCs and metamaterials to extend and control BGs. This has led to rapid advances in active functional metamaterials, enabling new capabilities such as selective wave filtering and nonreciprocity through static or dynamic modulation of material properties in space and time.

Numerous studies have investigated real-time tuning of BG widths and frequencies in PnCs and metamaterials. BG tunability primarily relies on variations in geometrical or material properties, often triggered by external stimuli, giving rise to the subfield of stimuli-responsive PnCs and metamaterials. Both Bragg and resonance-based BGs have been tailored through geometric modifications, such as altering the shape or symmetry of scatterers[70,71]. For example, **Fig. 1.5(a)** shows an adaptive elastic metamaterial with unit cells composed of metallic cores linked by elastomeric buckling-prone beams[71]. Fabricated from silicone rubber, the structure allows for significant deformation under compression, thereby enabling shape-dependent BG tuning observed in both the band structure and wave transmission. An alternative tuning strategy involves modifying the

intrinsic material properties using external fields. Though conceptually similar, this method can be more practical for real-world applications. As shown in the example of **Fig. 1.5(b)**, unit cells of a 2D lattice integrates electromagnets that connect or disconnect in response to an applied electrical current, allowing independent control of each unit cell and enabling BGs to be switched on or off[72]. This principle underlies the design of digitally tunable metamaterials for low-frequency waveguiding and vibration isolation. Other approaches for BG tuning include the incorporation of materials whose properties can be actively controlled via optical fields[73], electrorheological effects[74], electrical signals[75], piezoelectric circuits[76–78], magnetic fields[79,80] or temperature changes[81,82]. An example of tuning the BG with temperature involves a metamaterial composed of an array of resonators made from shape memory alloy beams. These beams bend in response to phase transitions induced by heating/cooling (**Fig. 1.5(c)**). This deformation significantly alters the local resonances, thereby modifying the band dispersion and, consequently, the frequency range and localization of the LR BGs as shown in the three right panels of **Fig. 1.5(c)**.

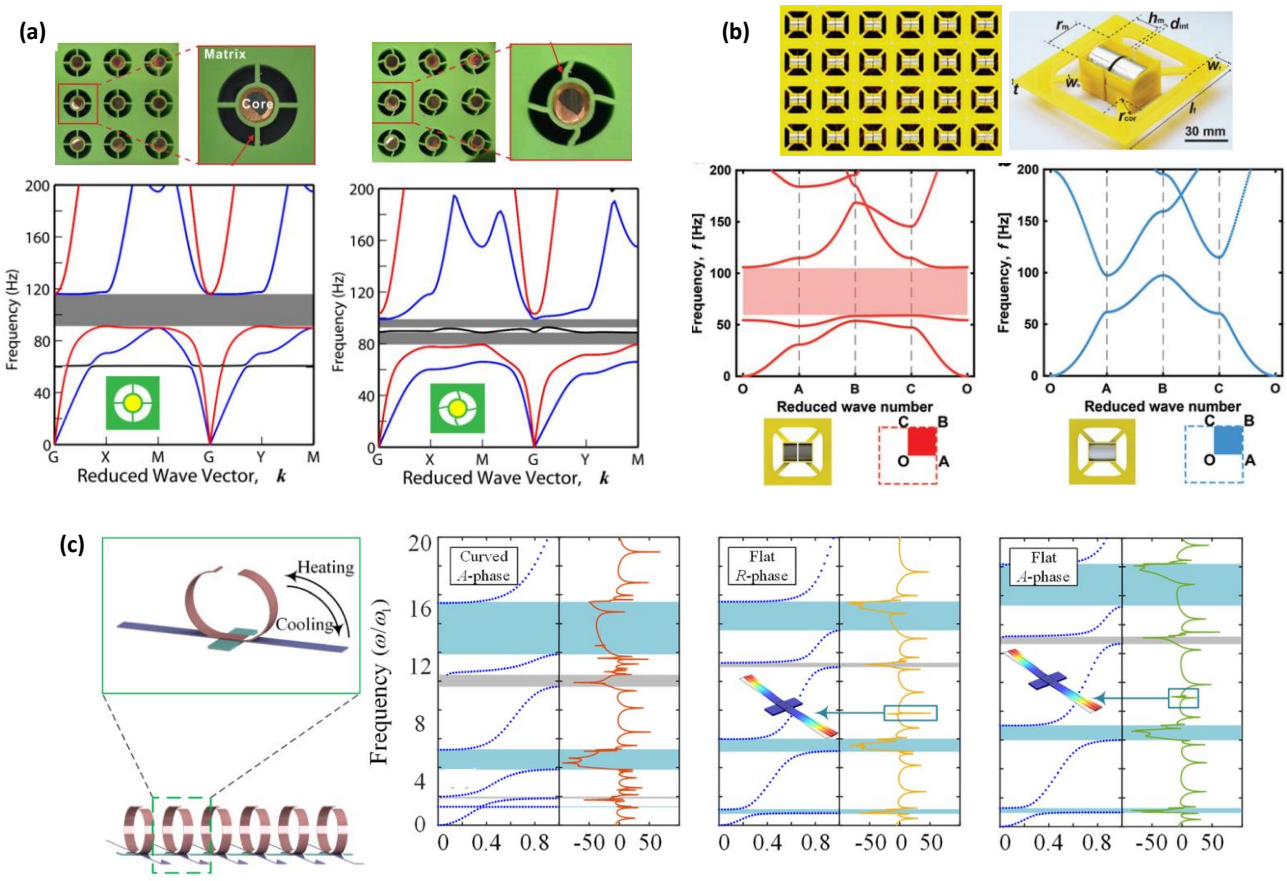

Fig 1.5. Examples of tunable elastic metamaterials. (a) A metamaterial comprises resonating units, each resonator consists of a metallic mass connected to the matrix through elastic beams[71]. When a compressive strain ε = -0.065 is applied in the vertical direction (right panels), buckling of the beams significantly alters the effective stiffness of the structural coating, which in turn changes the BG frequency (gray shaded regions) in the dispersion diagram (lower panels). (b) (Upper panels) Adaptive metamaterial where the unit cell made of a square frame, two pairs of beams, and two electromagnets that can attach or detach upon applying an electrical current[72]. (Bottom panels) Band structures of the metamaterial for detaching (left) and attaching (right) modes. (c) (left) metamaterial with shape memory alloy (SMA) beams that can bend under heat/cooling[82]. (Right three panels) band structures showing tunable BG (blue shaded areas) for A-phase curved, R-phase flat, and A-phase flat SAMs. A is for austenite and R is for rhombohedral.

Meanwhile, growing interest has emerged in using temporally modulated materials to break time-reversal symmetry, thereby enabling nonreciprocal wave propagation and unlocking a range of active metamaterial applications. This is achieved by deliberately varying effective mechanical properties such as stiffness, in time, in a fast manner allowing the design of materials that break wave reciprocity. ***Chapter 4*** of this manuscript presents a review of nonreciprocal phononic structures, along with our contributions to the design of compact metamaterials that enable unidirectional propagation of acoustic and elastic waves.

1.3 Perspectives for BG engineering in PnCs and metamaterials

The field of phononic BGs engineering has significantly advanced, not only in terms of fundamental understanding but also through technological integration with optomechanics, quantum systems, and topological physics. Various applications are now being explored, including GHz-scale devices, waveguides, mechanical logic circuits, vibration isolation, and energy harvesting. Emerging directions in topological BG engineering are particularly promising. Structures inspired by Z2 topological insulators, valley Hall systems, and higher-order topological states enable unprecedented localization and robustness of wave modes. For example, topological defects such as disclinations or dislocations can host localized states within the BG, which may serve as energy traps for highly sensitive sensors[83].

In parallel, optomechanical crystals operating at GHz frequencies have opened a new avenue where mechanical vibrations interact with photons. This has allowed researchers to demonstrate quantum behaviors, including optomechanical entanglement[23], quantum transduction[84], and quantum teleportation[85]. These advances offer a pathway toward integrated quantum systems that unite light and sound, though most demonstrations still rely on cryogenic conditions. The challenge remains to realize such effects at room temperature for practical applications.

3D architected metamaterials represent another major frontier. These complex structures, designed for dynamic control across multiple directions and frequency ranges, demand data-driven and inverse-design methods to navigate their vast design space. Traditional forward simulations often fall short due to the complexity of these systems. However, advances in additive manufacturing, including multi-material and piezoelectric printing[69,86], have made it feasible to fabricate these structures with high precision.

Beyond periodicity, quasicrystals and hyperuniform lattices are explored for their aperiodic order, which can still produce BG-like behavior. While these structures cannot be analyzed using conventional dispersion methods, frequency response analysis has shown that they can exhibit photonic and elastic BG, as well as strong wave localization[87–89]. Despite significant theoretical interest, experimental demonstration in elastodynamics remains limited, highlighting a rich area for future research.

A particularly innovative concept discussed is that of twisted bilayer PnC, inspired by the physics of twisted bilayer graphene. These systems consist of two phononic lattices layered with a relative twist angle and exhibit interlayer coupling. At specific configurations, such as those with even sublattice exchange (SE) symmetry, the structure can open up novel elastic BGs hosting higher-order topological states, like corner modes[90].

Furthermore, valley Hall edge states can emerge in frequency regimes not accessible to monolayer configurations, suggesting new forms of topological phononic heterostructures[91].

BGs for nonlinear elastic waves can be explored, especially through granular and deformable metamaterials. These platforms can support solitons and other strongly nonlinear waves, enabling technologies such as impact absorbers, mechanical logic switches, and non-destructive testing tools[92–94]. Recent work shows vector soliton propagation and even lattices with BGs tailored for solitons[95,96], paving the way for amplitude-dependent wave control in elastic systems.

Another exciting field to explore is elastic wave propagation in non-Euclidean geometries. Inspired by hyperbolic lattices in quantum electrodynamics and photonics[97–99], researchers are beginning to study wave dispersion in curved-space elastic lattices. Such systems, potentially realizable via origami-inspired architectures, could enable entirely new classes of metamaterials where geometry, not just material composition, governs dynamic behavior[100].

In summary, BG engineering in PnCs and elastic metamaterials is becoming a rich, multidisciplinary field at the crossroads of physics, materials science, data science, and quantum technologies. With the integration of topological design principles, machine learning-driven optimization, and advanced manufacturing, the control of elastic waves is expected to know advances that will sustain the field for decades, leading to transformative applications in sensing, communication, quantum devices, and energy systems.

Chapter 2: Planar ultra-thin metamaterials for acoustic wave manipulation

In this chapter, we focus on a class of metamaterials engineered in a planar geometrical configuration to be ultra-thin relative to the operating wavelength (i.e., thickness ≪ wavelength). In such cases, these structures are referred to as metasurfaces, as their minimal thickness allows them to be effectively perceived as surfaces at the wavelength scale. We present several examples of planar metamaterials we have designed and fabricated in recent years, targeting either broadband sound absorption or enhanced acoustic wave transmission, with applications in acoustic energy harvesting and transfer.

2.1 Hybrid metasurface for airborne-sound absorption

The development of ultra-thin engineered materials known as metasurfaces[101], has opened new avenues for achieving enhanced broadband sound absorption at deep subwavelength scales, which is highly sought in various fields, including room acoustics, automotive engineering, aeronautics, and aerospace. Conventional sound-absorbing materials such as foam, fiberglass, and mineral wool, are inherently limited by the dependence of their thickness on the wavelength of sound, which restricts their performance, particularly in the low-frequency range[102]. The emergence of acoustic metamaterials has revolutionized the field by enabling ultrathin metasurfaces with strong sound absorption at deep subwavelength scales[103–107]. However, achieving broadband high absorption in the low-frequency regime (below 200 Hz) remains a significant challenge, with the required physical thickness of the absorber being a major limiting factor[104]. One of the initial strategies to address this involved integrating thin membranes into a rigid grid panel[108,109]. While effective, these membrane-based systems are highly sensitive to mechanical tension of the used membranes, complicating their fabrication and consistency. An alternative approach employs a perforated panel coupled with a coiled planar resonator, allowing the overall structure to remain compact in the direction normal to the panel surface[103,110,111] (**Fig. 2.1(a)**). This configuration can achieve near-perfect absorption at a deep subwavelength scale, though typically over a narrow frequency band centered around the structure's resonance (**Fig. 2.1(b)**).

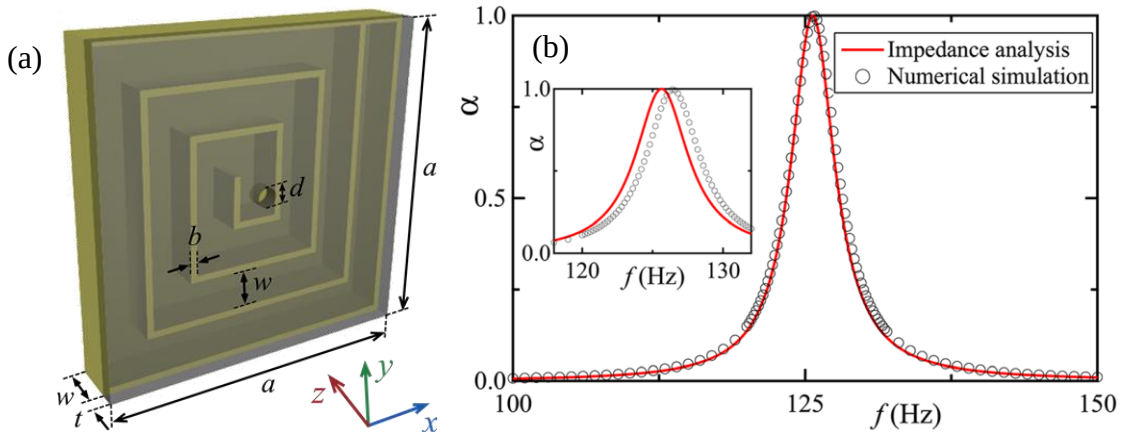

Fig. 2.1. (a) The acoustic metasurface absorber composed of a perforated plate (transparent gray region) (thickness *t*) with a hole (diameter *d*) and a coiled air chamber (thickness *w*) (yellow region). Several solid

beams are used to form the coplanar air chamber. (b) The absorption coefficient, α, of the presented metasurface with geometrical parameters (d = 3.3 mm, t = 0.2 mm, a = 100 mm, w = 12 mm, and b = 1 mm). Total absorption is realized at 125.8 Hz[103].

Broadband sound absorption was later achieved using super-cells composed of multiple unit cells with coiled cavities, whose resonance frequencies were carefully selected to enable mutual coupling, thereby enhancing absorption over a broad frequency range[105–107,112]. Building on this design strategy, we recently introduced an innovative design that significantly extends the absorption bandwidth beyond the limits of classical coupled-cavity systems without increasing the planar footprint of the metasurface. This advancement involves a hybrid configuration, in which four coupled coiled resonators are additionally linked to carefully designed thin planar back-cavities arranged in the normal direction[113] (**Fig. 2.2 (a)**). This hybrid coupling mechanism enables a substantial bandwidth enhancement: an increase in absorption bandwidth below 200 Hz is achieved while maintaining a subwavelength total thickness of only 50 mm (λ/51). **Figure 2.2(a)** illustrates the geometry of the hybrid metasurface, and **Fig. 2.2(b)** compares its absorption performance with that of a conventional four-coupled-resonator metasurface (without the back cavity). The hybrid design achieves a 200% wider absorption band at a 0.5 absorption coefficient, demonstrating its superior broadband capability.

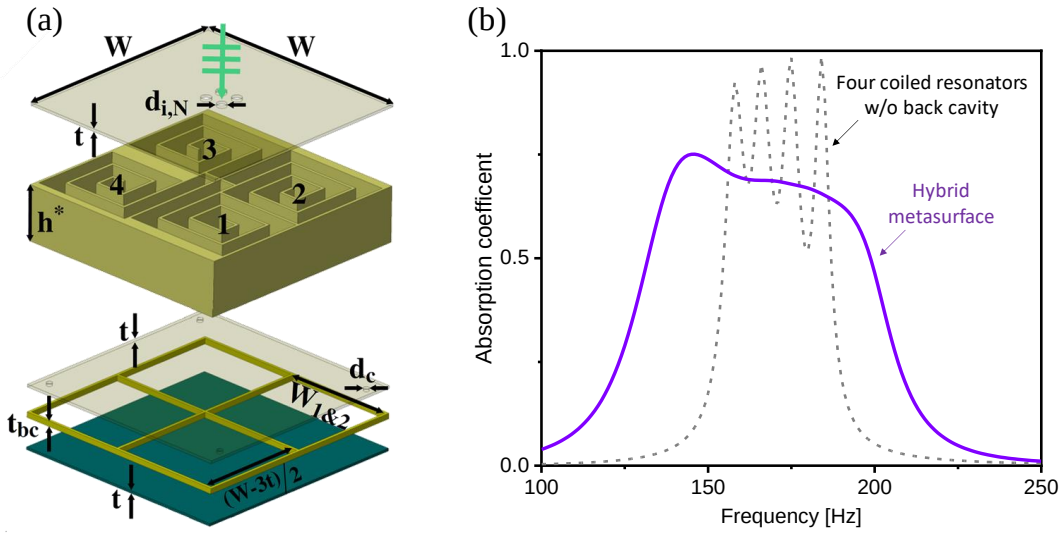

Fig. 2.2. (a) A hybrid metasurface made of four coiled resonators with individual back-cavities. (b) Absorption spectra for both the designs with and without the back cavities[113].

2.2 Plate type metamaterials for vibration mitigation and energy harvesting

With growing environmental concerns over fossil fuels, clean and renewable energy sources have drawn global interest. Sensors and actuators are now central to modern life, making it essential to develop sustainable power solutions for these devices. MEMS-based sensors, for example, consume very little energy, typically under 100 μW for devices smaller than 1 cm³. Among emerging sources, sound energy, though often seen as noise, offers a clean and renewable option for powering microelectronic systems[114]. However, due to its low power density, sound must first be confined or localized to enable efficient conversion into electrical energy via piezoelectric, electrostatic, or electromagnetic mechanisms. Traditional resonators like Helmholtz[115,116] or tube[117] have been used for acoustic energy harvesting (AEH). More recently, PnCs and acoustic metamaterials have introduced novel wave manipulation strategies, allowing both sound insulation and energy concentration

for harvesting. By creating defects within their structure, PnCs and metamaterials can strongly confine acoustic energy by the creation of a cavity mode within the BG. This energy is then extracted using a piezoelectric cavity. While early AEH systems relied on Bragg BGs[118], targeting low frequencies (e.g., ~1 kHz) lead to large structures, limiting their use in compact devices. Acoustic metamaterials overcome this with their ability to LR BGs at deep-subwavelength scales. We have demonstrated that planar AMMs can achieve high strain energy confinement and low sound transmission loss at low frequencies[119–121], making them promising for both sound insulation and AEH. Their key advantage lies in their scalable design, where the target frequency range can be tuned by simply adjusting the mechanical properties of the resonators.

To demonstrate the use of planar metamaterials for AEH, we consider a pillared metamaterial plate[122]: a plate with an array of resonating pillars (**Fig. 2.3(a)**). These pillars generate a LR BG in the structure's dispersion (green shaded area in **Fig. 2.3(c)**). Introducing a defect by removing four pillars creates a flat-band defect mode within the BG around 2.26 kHz, as shown in **Fig. 2.3(c)**. An incident acoustic wave excites this defect mode, leading to strong strain energy confinement within the defect region (**Fig. 2.3(e)**), which is then harvested via a piezoelectric patch (PZT). **Figure 2.3(d)** shows a dip in sound transmission loss spectrum at the defect frequency, confirming mode excitation. Part of this transmitted energy is converted to electricity using the PZT connected to a resistive load, with optimal energy output at ~38 kΩ (**Fig. 2.3(e)**). The practicality of this design has also been experimentally validated for other defect configurations[123].

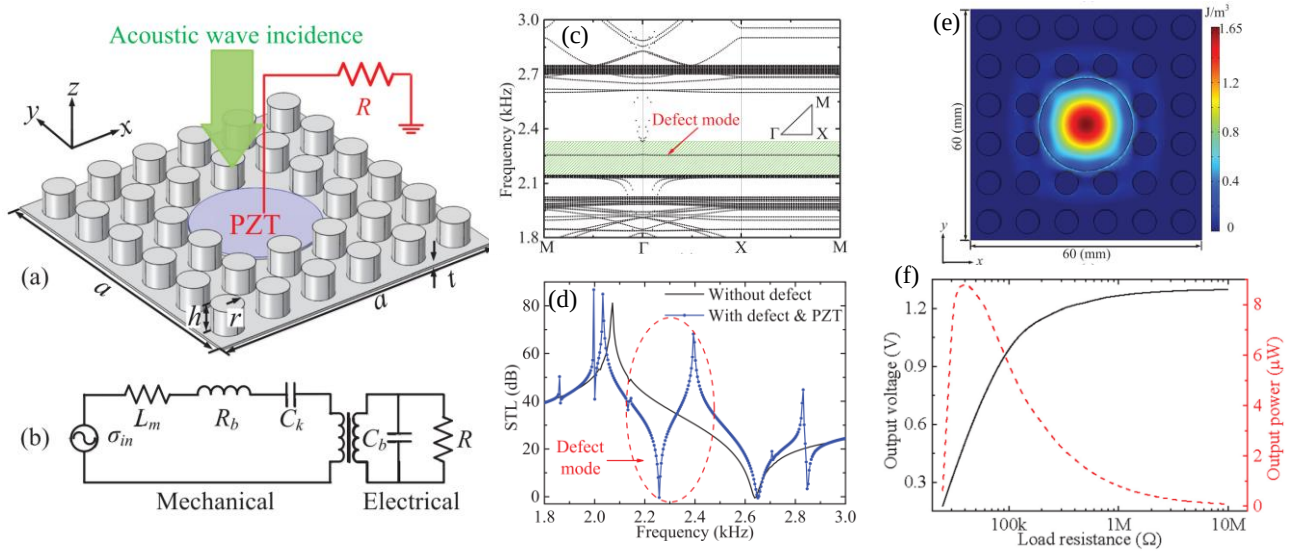

Fig. 2.3. (a) Sketch of the AEH based acoustic metamaterial system composed of a supercell of arrays of pillars with a defect created by removing four pillars[122]. A piezoelectric patch, connected to a lead resistor, is glued into the defect space. (b) Equivalent circuit representation of the piezoelectric converter with a resistive load *R*. (c) Computed band structure of the system. (d) Sound transmission loss as function of the frequency through the planar metamaterial. (e) Strain energy density distribution of the structure at the cavity mode's frequency (2257.5 Hz). (f) Output electrical voltage magnitude (black solid line) and power (red dashed line) from the circuit versus the load resistance *R* at the defect mode's frequency (2257.5 Hz).

While this metamaterial design approach allows for more compact devices compared to PnC platforms in acoustic energy harvesting, it lacks precise control over the defect mode within the bandgap. Typically, the presence of a defect mode is dictated by the number of the removed pillars, which limits the ability to fine-tune the defect's spatial extent—posing challenges for device miniaturization, particularly at low frequencies

(around 400 Hz). An alternative strategy for controlling defect size and tuning the cavity mode involves modifying the mechanical properties (mass and stiffness) of one or more pillars within the lattice, rather than removing them. This method introduces additional design flexibility, enabling more precise shaping of the cavity mode while preserving the overall geometry of the metamaterial. We have demonstrated the effectiveness of this approach in our previous work[124].

2.3 Acoustic metamaterial plate for contactless wireless ultrasound energy transmission and data transfer

Enhancing sound transmission at specific frequencies has applications beyond energy harvesting, as it can also address critical industrial challenges. One key example is wireless power and data transfer (WPDT) through sealed or enclosed structures to power and communicate with sensors, which is essential for specific environments like nuclear canisters[125], pipelines[126], enclosed engines[127], aircraft fuselages[128], and implantable medical devices[129]. WPDT removes the need for wiring or batteries, which are often bulky or impractical in such settings. Inductive Power Transfer (IPT), a widely used WPDT method, employs AC-driven coils to generate electromagnetic fields for wireless energy transfer[130]. While IPT is effective for devices like phones and drones, it suffers from a major limitation: poor performance through metallic barriers due to Faraday shielding. To overcome this, researchers have explored wireless ultrasound power and data transfer (WUPDT) as an alternative[131]. This approach uses piezoelectric transducers to convert mechanical vibrations into electrical signals and vice versa. Compared to IPT, WUPDT offers longer transfer distances, smaller receivers, lower power consumption[131], and most importantly, effective transmission through metal, making it a practical solution where IPT fails.

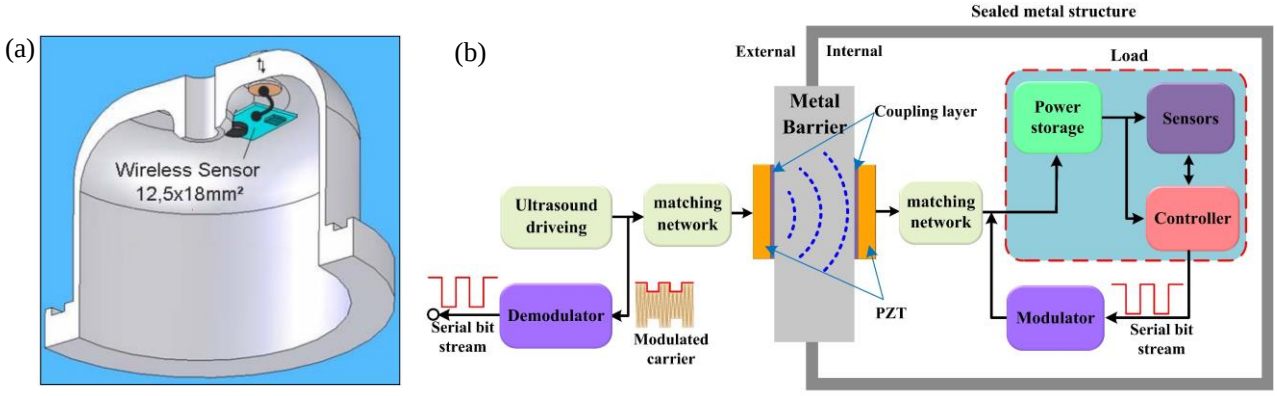

Fig. 2.4. (a) Schematic view of an example of a sealed container (hydraulic accumulator) where a wireless sensor is mounted with ultrasound powering and data transfer system. (b) Example of an ultrasonic transmission system block with piezoelectric transducers mounted in contact with the container wall. (PZT : Lead zirconate titanate transducer)[132].

WUPDT operates using a pair of piezoelectric transducers, an emitter and a receiver, to transmit and detect ultrasound. As shown in **Fig. 2.4**, a sensor inside a sealed container communicates through a metallic wall via ultrasound transducers placed in contact with both sides[132] (**Fig. 2.4(a)**). The emitter converts electrical signals into ultrasonic waves (stress waves), which travel through the barrier and are converted back into electrical signal by the receiver. While previous efforts have focused on optimizing transducers and circuitry, direct contact between transducers and the metal barrier remains essential. This is typically achieved using polymeric

coupling layers to improve acoustic impedance matching. However, these layers degrade over time and are especially vulnerable to harsh environments[133] (e.g., high temperatures), leading to acoustic performance loss or delamination. To address this, we have developed a contactless WUPDT approach using pillared acoustic metamaterial plates, enabling ultrasound transmission through acoustically opaque barriers without relying on fragile coupling layers[134].

The pillared acoustic metamaterial consists of a steel plate (metal barrier) patterned with a square lattice of cylindrical pillars (**Fig. 2.5(a)**). Each pillar includes a neck (diameter d_N and height h_N), a larger cap (diameter $d_C > d_N$, height (h_C), and a tapered section (h_T) for easier fabrication. Acting as spring–mass resonators, these pillars can be geometrically tuned to match the transducer's working frequency. The barrier (plate) and pillars are all made of steel (steel US316L). When ultrasonic waves impinge upon the plate, the pillars resonate and radiate secondary waves, enhancing the transmission (**Fig. 2.5(b)**). Momentum conservation ensures continuity of the tangential wave vector $\boldsymbol{k}_{||} = (k_x, k_y)$, enabling propagating elastic waves inside the plate. Band structure analysis (**Fig. 2.5(c)**) reveals flat modes near 460 kHz at the Γ point: two degenerate in-plane modes (γ_1, γ_2) and one out-of-plane mode (δ). At normal incidence, only δ, featuring axial elongation, is excited, resulting in strong sound transmission. Within 300–600 kHz, the bare plate transmits <2% power due to impedance mismatch with water, while the metamaterial achieves 72% at 460 kHz (**Fig. 2.5(d)**). Angle-resolved transmission (**Fig. 2.5(e)**) shows robust performance (>70%) across incident angles ranging from 0° to 60°, with optimal frequency remaining near 460 kHz.

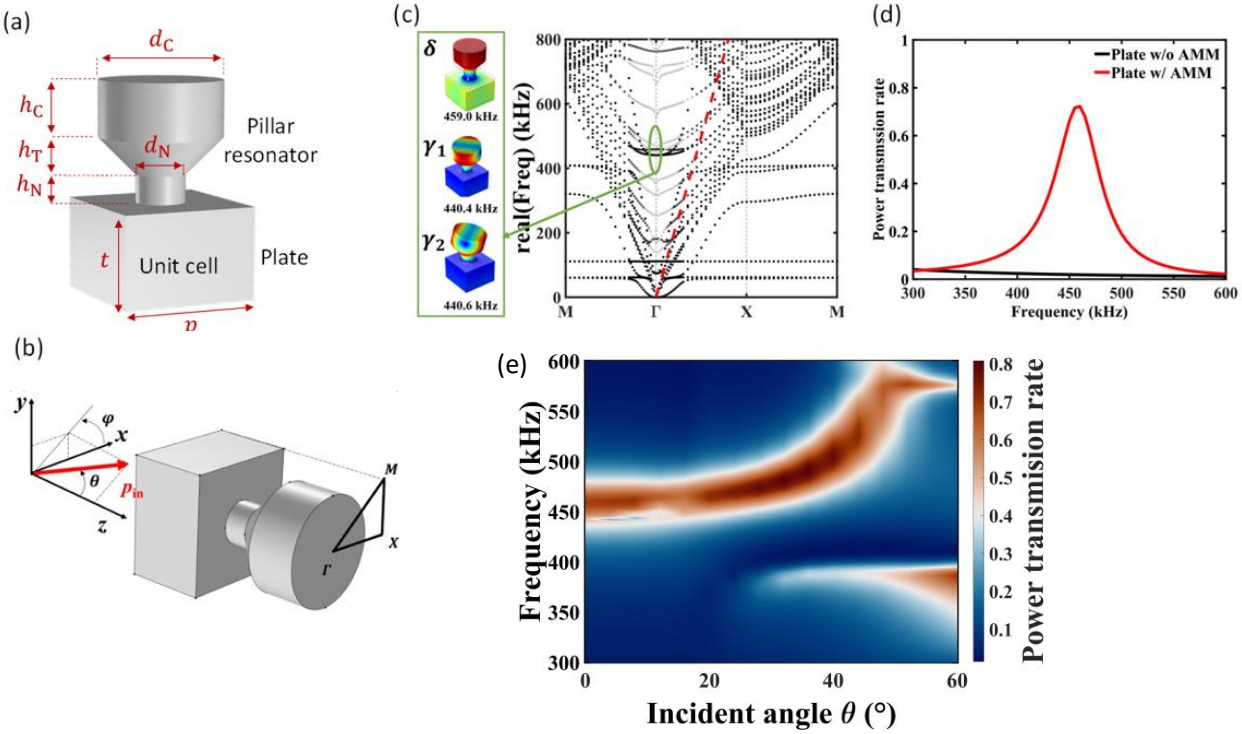

Fig. 2.5. (a) The unit cell of the pillared acoustic metamaterial (AMM) showing (a) the shape/dimensions and (b) the directions, angles for incident pressure wave p_{in}, and the irreducible Brillouin zone. The geometrical parameters are: $p = 1.5\ mm$ mm and $d_N = 0.54\ mm$, $d_C = 1.35\ mm$, $h_N = 0.3\ mm$, $h_C = 0.405\ mm$, and $h_T = 0.615\ mm$. (c) The band structure along the MΓXM directions where the modes are displayed by the dots. The gray ones cannot be excited by acoustic waves from water. The green ellipse encompasses three propagating modes corresponding to δ, γ_1 and γ_2. The left panel shows the distribution of the displacement magnitude $\|\boldsymbol{u}\|$ for these modes. The red dash line is the sound line in water. (d)

Ultrasound power transmission rate for the bare plate and the acoustic metamaterial for normal incidence. (e) Power transmission rate as a function of the incident angle θ when $\varphi = 0^o$.[134]

The waterborne scenario is experimentally validated through comparison with numerical simulations, utilizing advanced 3D metal printing technology. **Figures 2.6(a)** and **(b)** present both a schematic and a photograph of the experimental setup, including a close-up inset of the metamaterial plate pillars. **Figure 2.6(c)** compares the simulated and measured power transmission rates for the plate with and without the metamaterial. The measured transmission for the bare 1-mm thick plate is around 2% at approximately 442 kHz (black dots). By contrast, when the metamaterial is added atop the plate, the transmission significantly increases to 65.5% at 442 kHz, with a half-power bandwidth of 33 kHz (red dots). Aside from a minor frequency shift, likely caused by fabrication imperfections, the experimental and simulation results align well, clearly demonstrating the enhanced power transmission enabled by the AMM.

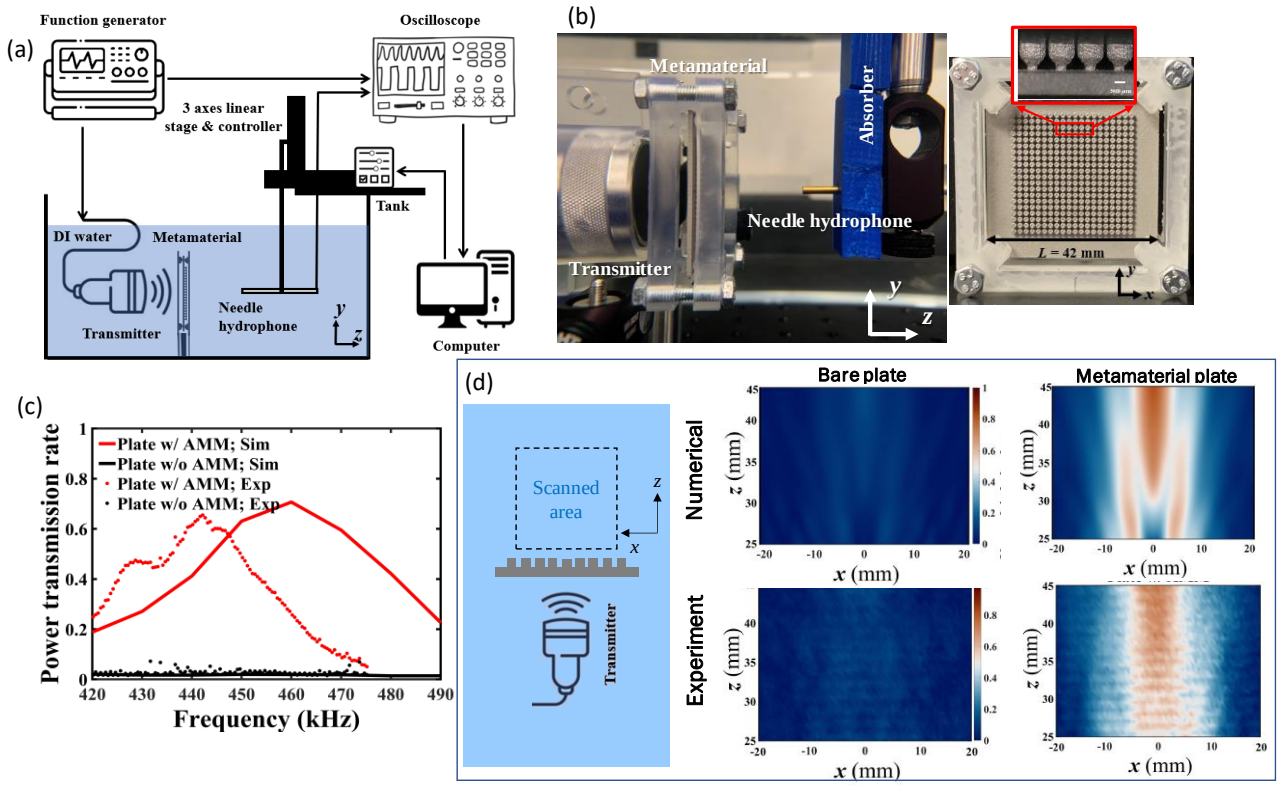

Fig. 2.6. (a) Schematic and (b) photo of the experimental setup. (Right panel in (b)) Fabricated plate with the metamaterial with the close-up view of the pillars (inset). (c) Comparison of simulated (solid line) and measured (dots) power transmission rates for the cases of bare plate (in black) and the metamaterial plate (in red). (d) The spatial distribution of the transmitted pressure fields from numerical simulations (at 460 kHz) and experimental measurements (at 442 kHz) demonstrating the enhanced transmission by the metamaterial in comparison to the case of bare plate.

With the proven ability to enhance transmission through the metal wall, the pillar-based metamaterial is used to implement a wireless and contactless ultrasound power transfer (WCUPT) system. **Figures 2.7(a)** and **(b)** show the schematic and photo of energy harvesting through the metal wall placed at z = 45 mm, where a receiver collects the transmitted ultrasonic power. The enhanced ultrasound energy charges capacitors and lights a commercial LED (**Fig. 2.7(d)**), which is impossible through a bare plate. At 445 kHz continuous ultrasound excitation, the receiver's AC output is converted to DC via a full-bridge rectifier. **Figure 2.7(c)** displays the voltage across a 220 μF capacitor over 400 seconds for four cases: "no plate", "plate with AMM",

"plate without AMM" at 4.4 Vpp input, and "plate without AMM" at 20 Vpp input (AMM refers to acoustic metamaterial). The metamaterial plate clearly enables faster charging than the bare plate, despite the bare plate using a 4.5 times higher input voltage. Since the LED requires about 2 V, seven capacitors in series charged to 2.22 V in the "no plate" case, storing 77.4 μJ over 424 seconds (182 nW output). In the "plate with AMM" case, ten capacitors reached 2.1 V (116 nW output), successfully lighting the LED (**Fig. 2.7(d)**). This output matches well with the measured 65.5% power transmission in **Fig. 2.6(c)**. Conversely, the "plate without AMM" case only reached 1.2 V on ten capacitors, failing to power the LED even at 20 Vpp excitation.

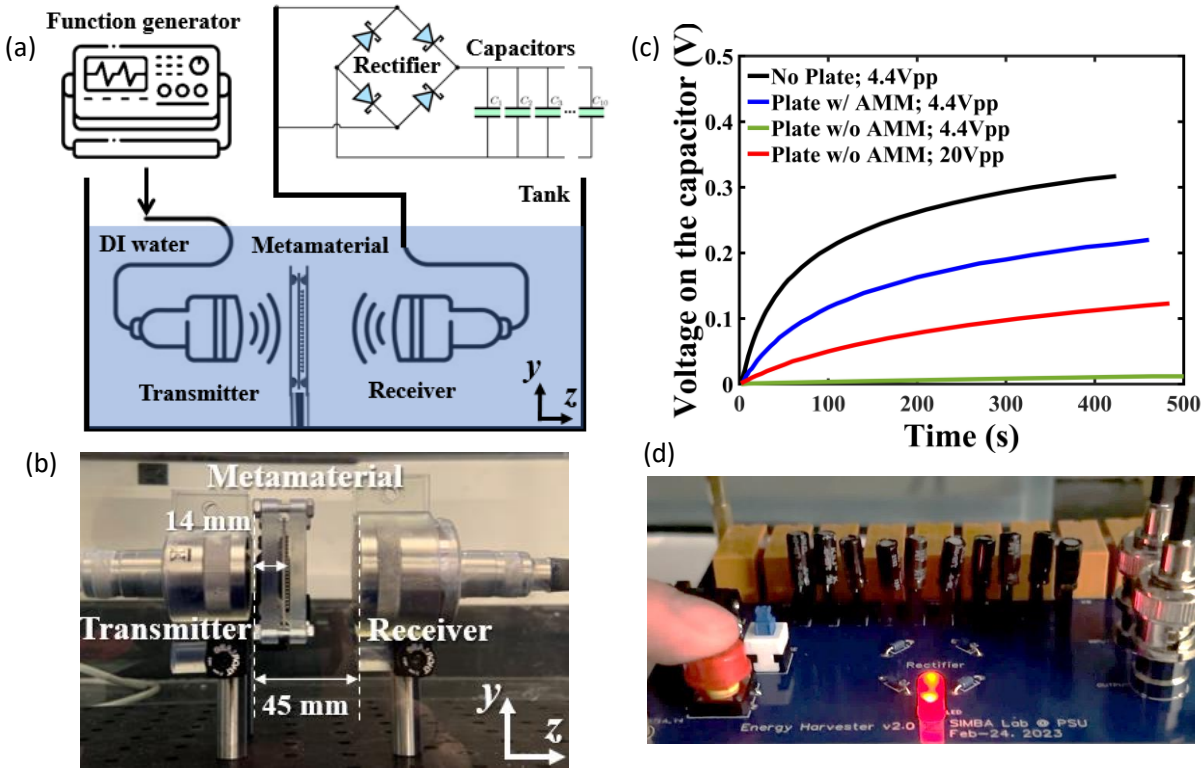

Fig. 2.7. Experimental results of WCUPT through a metallic wall using the pillar-based metamaterial. (a) Schematic and (b) photo of experimental setup. The enhanced ultrasonic transmission is collected by a receiver to charge capacitors under an excitation of 445-kHz continuous-mode ultrasound. (c) The charging time dependence of voltage on a 220 μF capacitor for four configurations: an input voltage of 4.4 Vpp on the transmitter for "no plate" (black curve), "plate w/ AMM" (blue curve), the "plate w/o AMM" (green curve), and an input voltage of 20 Vpp on the transmitter for "plate w/o AMM" (red curve). (d) Photo of the LED lighting.

In addition to enabling contactless power transfer, wireless contactless data transfer has also been successfully demonstrated. Burst-mode sinusoidal signals using amplitude shift-keying (ASK) modulation are applied to the transducer with a low input voltage of 25 mV to transmit encoded binary data. As an example, a 15-bit data string across 15 columns is used to create an image of "PSU" (**Fig. 2.8(a)**). This figure illustrates the encoding and decoding process for WCUDT: the original 15-bit binary signal is framed by start bits (100) and stop bits (001), producing a 21-bit sequence (15 + 3 + 3). **Figure 2.8(b)** shows the transmitted signal waveform (orange curve), which visually represents the quality of the signal. When the barrier includes the metamaterial, the received digital signal experiences only minor distortion, and the decoded data closely matches the transmitted sequence, allowing successful reconstruction of the PSU image. Conversely, without the AMM (bare plate), the transmitted signal is weaker and significantly affected by noise, preventing proper image recovery.

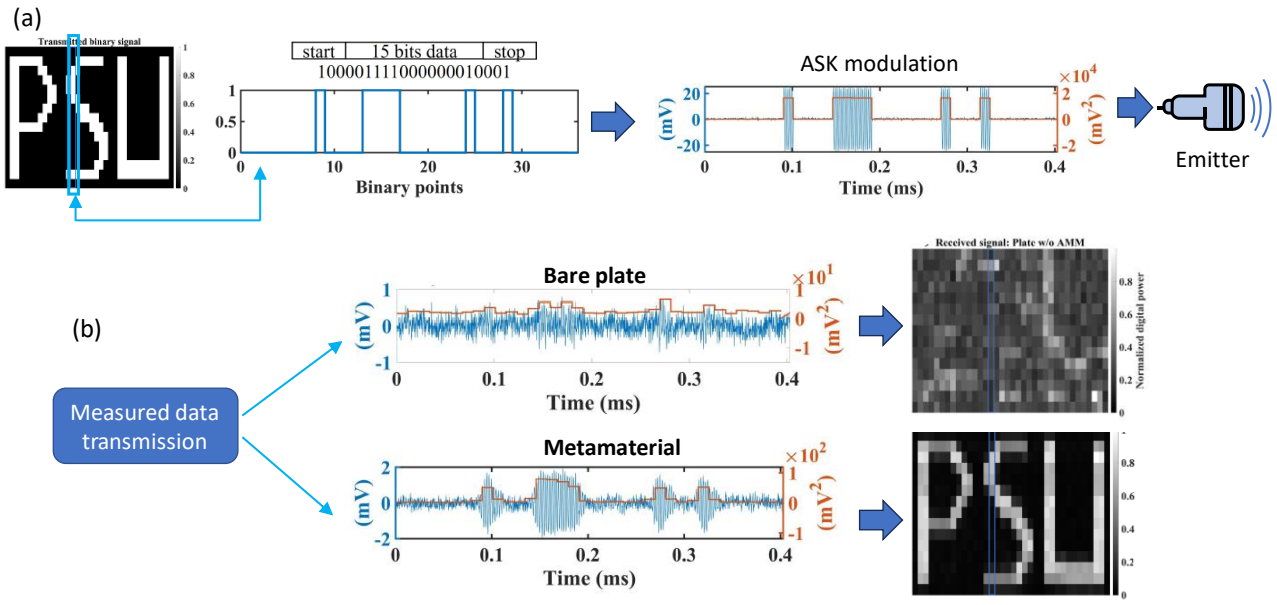

Fig. 2.8. Experimental results of wireless and contactless ultrasonic data transmission of a binary image of "PSU". (a) The PSU image, composed of 15 × 36 pixels, is encoded into binary signals of "0" and "1. The transmission of binary data using ASK modulation: a 15-bit binary signal, embedded within the start bits (100) and the stop bits (001), is transformed into digital signal before being transmitted through a transducer, in which each bit is represented by five cycles of sine waves at 445 kHz. (b) The received time-domain digital signal for the "bare plate" and the "plate with the AMM."

In summary, this pillar-based acoustic metamaterial enables wireless ultrasound power transfer and data transmission through a metallic barrier, all in a fully contactless manner, an issue previously considered highly challenging. The design and optimization of the metamaterial follow a deterministic approach involving band-structure theory and transmission analysis. This work not only broadens the scope of acoustic metamaterial research and advances 3D metal printing technology but also paves the way for the next generation of ultrasonic power and data transfer systems capable of operating through metal walls.

2.4 Engineering ultras-thin metamaterials for broadband underwater sound absorption

The development of innovative materials for underwater sound absorption is important for protecting marine life from intense noise generated by ships, pile driving, and high-power naval sonars[135]. Unlike in air, acoustic pressures in water is orders of magnitude higher (from 10 kPa to 1 MPa), making sound attenuation significantly more challenging. Underwater sound absorption primarily relies on wave energy dissipation through viscoelastic losses in damping materials. Early designs featured viscoelastic coatings such as PDMS, embedded with air-filled cavities[136–138], high-density rigid spheres[139,140], or softly coated resonant units[141]. These materials are selected to match the acoustic impedance of water and minimize reflection. Air-cavity-based structures achieve near-total absorption at high frequencies (MHz), while systems incorporating high-density spheres operate effectively at lower frequencies (below 10 kHz), using resonance to amplify viscoelastic losses. However, resonance-based absorption is inherently narrowband, and achieving broadband performance often requires increasing the metamaterial thickness (typically exceeding 15 cm) to ensure effective energy dissipation.

Beyond traditional structures with embedded resonant units, we have recently developed a new class of mechanical metamaterials that leverage elastic wave mode conversion to achieve broadband, subwavelength underwater sound absorption. The proposed meta-structure consists of a bilayer system (**Fig. 2.9**), combining a viscoelastic rubber layer with a solid meta-converter specifically engineered to convert longitudinal (L) waves into shear (S) waves. Knowing that S waves have significantly shorter wavelengths than L waves, the resulting decay length due to viscoelastic losses is much smaller. This key advantage enables a substantial reduction in the overall thickness of the absorber. Since acoustic waves in water are purely longitudinal, the incident wave first excites L waves in the rubber layer, which then propagate into the meta-converter. There, Fabry–Pérot resonance in reflection facilitates efficient conversion from L to S waves (as schematically described in **Fig. 2.9(a)**). As S waves cannot propagate in water, they are confined within the elastic layers, undergoing multiple reflections and resulting in strong energy dissipation over a short distance.

To optimize this wave conversion and energy loss, we developed a semi-analytical model and a full numerical framework to fine-tune the effective elastic properties of the meta-converter. From these effective properties, the meta-converter's geometry was generated using topology optimization (inset, **Fig. 2.9(b)**)[142]. **Figure 2.9(b)** shows the absorption coefficient (solid green curve) and the mode conversion efficiency R_{LS}, representing the rate of L-to-S wave conversion across the meta-converter. The structure demonstrates high R_{LS} and broadband sound absorption within the 2–6.5 kHz range, confirming that strong mode conversion directly correlates with enhanced acoustic absorption. **Figure 2.9(c)** illustrates finite element simulations of the reflected pressure field in water and the displacement amplitude within the bilayer system (rubber/meta-converter) at 7.15 kHz, a frequency exhibiting strong absorption. The results show pronounced shear wave activity within the solid layers and a significant reduction in reflected acoustic pressure in water. Finally, successful experiments validated the performance of this elastic wave conversion-based metamaterial, demonstrating its feasibility for compact, broadband underwater sound absorption[143] (**Fig. 2.9(d)**).

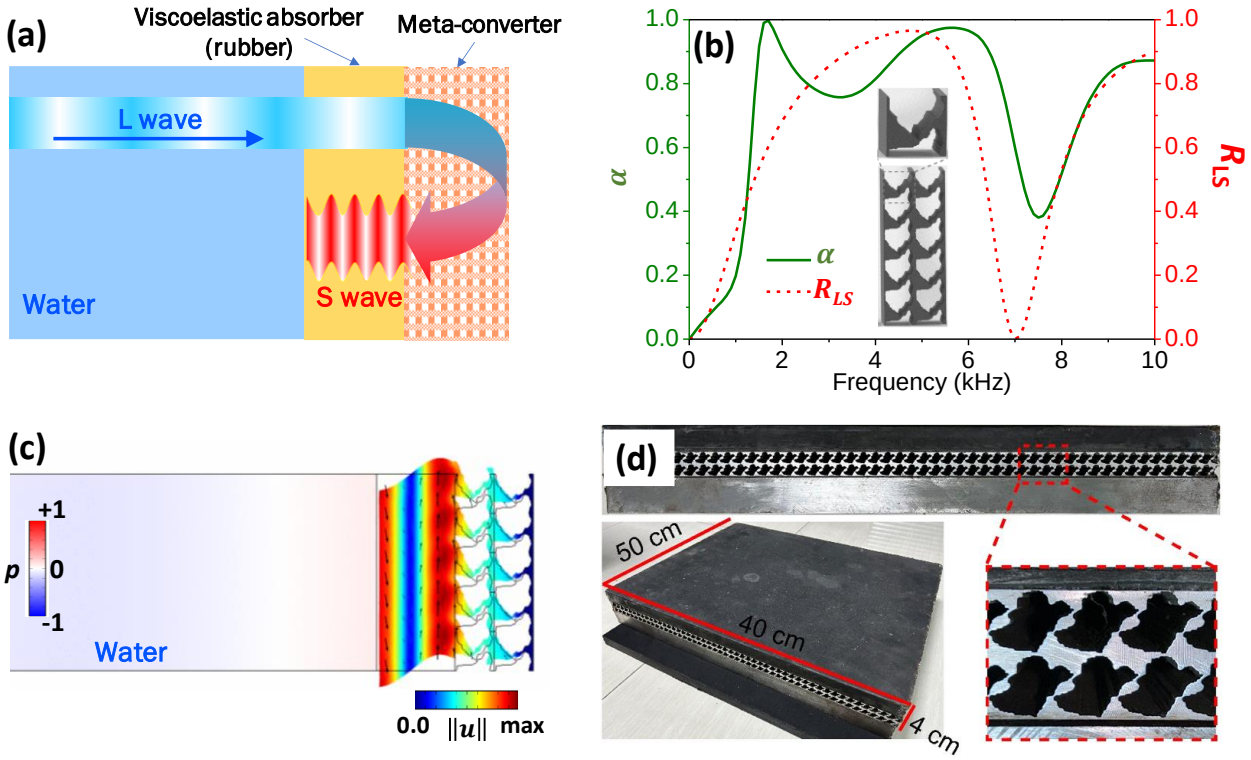

Fig. 2.9. (a) Schematic of the sound absorption mechanism based on elastic mode conversion. Incoming pressure wave in water excites L waves in rubber, which are converted to S waves in reflection within the meta-converter. The shear wave gets trapped and attenuated within the viscoelastic layer (rubber). (b) Absorption coefficient α and mode conversion L to S rate R_{LS} as function of the frequency. Inset is the meta-converter design made of air holes in aluminum, designed by topology optimization from the effective mechanical properties. (c) Wave fields within the system: pressure wave p in water and displacement field amplitude in the metamaterial-based bilayer absorber. (d) fabricated sample of the bilayer metamaterial absorber.

Chapter 3: On-chip metamaterials for enhanced surface acoustic wave sensing

Over the past decade, growing interest was brought to PnCs and metamaterials at megahertz to gigahertz frequencies, driven by advances in micro- and nano-fabrication enabling microscale phononic structures. Key applications include broadband wireless communication, optomechanics, and controlling thermal phonons to engineer material thermal conductivity and thermoelectric properties. Another emerging area is integrating PnCs and metamaterials in microfluidic devices for cell manipulation, stimulation, mechanobiology, and ultrasensitive sensing down to single molecules. This chapter presents our recent work on embedding PnC and metamaterials into microsystems, focusing on surface acoustic wave (SAW) devices. We investigate how these structures manipulate surface waves, starting with SAW dispersion in phononic architectures, then showing how PnCs produce high-Q elastic modes efficiently excited by SAWs, and finally demonstrating experimental SAW devices with metamaterials for improved sensing.

3.1 Pillared elastic metamaterials for surface acoustic wave control

Driven by applications in SAW sensing and filtering, several studies have examined SAW dispersion in PnCs and metamaterials. Special focus was given to designing micro-pillar arrays on semi-infinite substrates to achieve strong SAW dispersion. A 2D array of cylindrical pillars lead to the creation of phononic BGs for SAW due to pillar's resonance modes coupled with surface waves below the sound cone[144–146]. In contrast, periodic holes/or embedded material units cause Rayleigh wave scattering that leaks part of the surface wave energy into the bulk, quickly lowering the transmission at the surface of the substrate. To illustrate these behaviors, **Fig. 3.1** compares three cases: arrays of finite depth holes in a substrate, finite depth embedded material on the substrate, and array of pillars deposited on the surface[147]. The band structures calculations show that while all have surface modes below the sound line, only pillar arrays exhibit slow modes with near-zero group velocity at the Brillouin zone edges X and M, and clear bandgaps (highlighted in cyan in **Fig. 3.1(b)**). Displacement maps reveal elastic energy confined mainly within the pillars, minimizing the acoustic energy penetration to the substrate. Since these slow modes arise from pillar resonances at lower frequencies, the SAW wavelength exceeds the periodicity, producing subwavelength BGs. In the following sections, we explore leveraging pillar-array metamaterials to enhance SAW sensing.

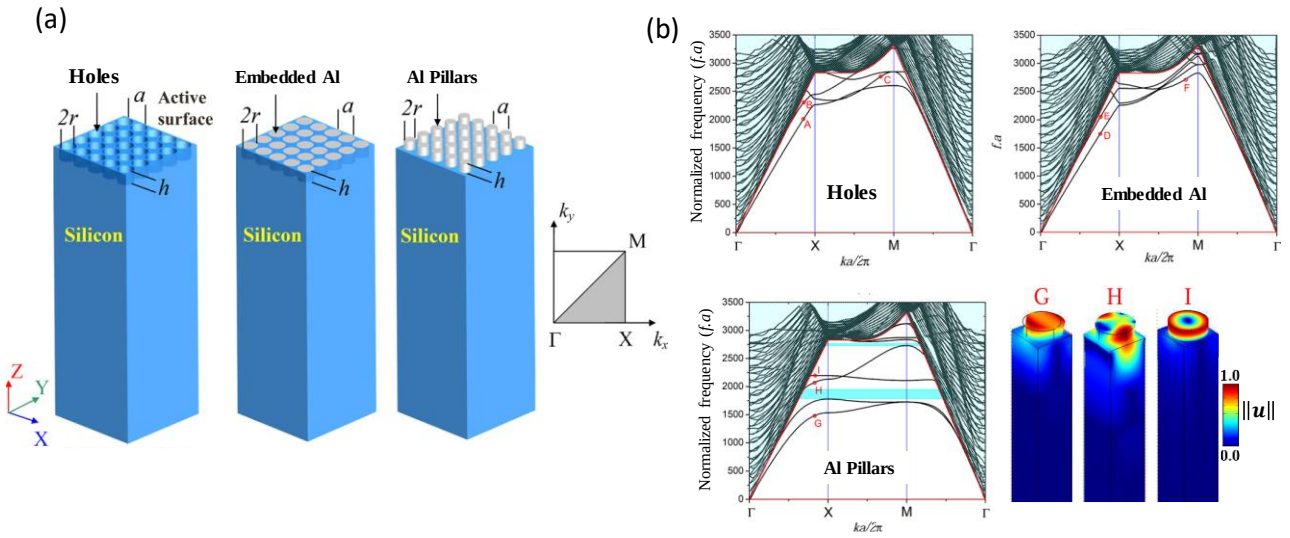

Fig. 3.1. (a) Schematic view of the three phononic structures made of square lattices of scatterers arranged on substrate: holes in silicon substrate, embedded aluminum scatterers in silicon substrate, and aluminum pillars on a silicon substrate. (b) Band structures of the investigated phononic structures. The dashed cyan region represents the sound cone of silicon substrate. The color maps represent the amplitude of the displacement field of some guided surface modes indicated in the band structures in the case of pillars[147].

3.2 Love wave control with pillared phononic metamaterial

SAW sensing has known major advances in the last decades, with devices emerging as cost-effective tools for real-time biomolecule detection[148]. Molecular binding events at the surface are tracked by measuring wavelength shifts, primarily caused by surface wave velocity changes due to mass loading. SAW devices offer advantages such as easy miniaturization, lab-on-a-chip integration, flexible thin-substrate design, and wireless operation for remote sensing[149,150]. However, their sensitivity remains limited and still "lags" behind cutting-edge optical technologies, especially for detecting small numbers of molecules. To enhance sensitivity of SAW sensing, we introduced a novel design methodology using phononic micro-pillars-based metamaterials. The detection mechanism relies on phononic micropillars acting as resonators that can be excited by Love waves which are used for chemical and biological sensing due to their high mass sensitivity and low energy loss in liquids[151].

We have theoretically investigated the mass sensitivity of a metamaterial-based Love SAW (LSAW) structure, which incorporates resonant phononic pillars exhibiting spectrally narrowband responses and strong local field confinement[55]. Each pillar is engineered from a phononic architecture consisting of alternating layers of tungsten and silica (**Fig. 3.2(a)**). This configuration enables the formation of BGs within which highly confined resonant modes can be localized—particularly near the pillar's surface. The design process begins with the analysis of the band structure of an infinite periodic microwire composed of alternating tungsten and silica layers, as illustrated in **Fig. 3.2(a)**. The corresponding band diagram in **Fig. 3.2(b)** reveals a broad BG extending from 193 MHz to 323 MHz (highlighted in cyan). From this idealized infinite structure, we derive a finite phononic pillar composed of five layers, with silica layers positioned at both ends (**Fig. 3.2(c)**). Assuming the base of the pillar is fixed, we demonstrate that such a configuration supports resonant modes in which mechanical vibrations are predominantly confined at the free end, primarily within the terminal silica layer (**Fig. 3.2(c)**). Three distinct localized modes emerge within the BG: a flexural mode (F), a torsional mode

(T), and an elongation (or compressional) mode (E). The frequencies of these modes can be tuned by adjusting the thickness h_T of the top free silica layer.

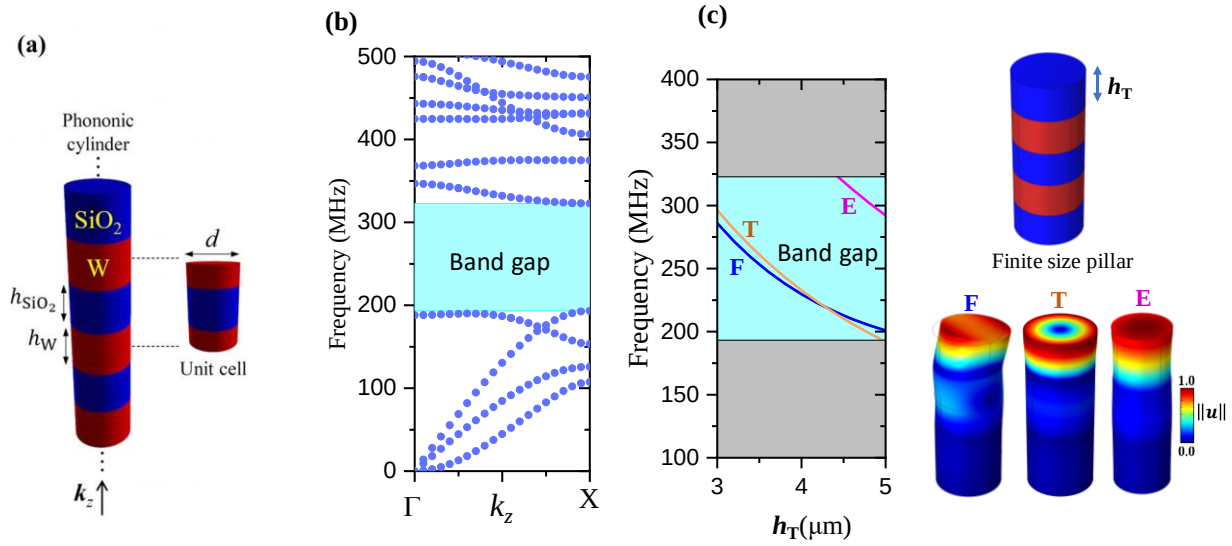

Fig. 3.2. (a) Phononic pillar made of alternating silica and tungsten (W) layers. (b) The band structure calculated along the k_z direction for $h_w = h_{SiO_2} = 3\ \mu m$ and $d = 6\ \mu m$. (c) Finite size phononic pillar made of alternating five layers of silica and tungsten where the bottom surface of the lower silica layer is fixed. The curves display the eigenfrequency modes of the finite phononic pillar as function of the height of the top free silica layer. Three modes appear inside the BG (cyan filled region): flexural (F), torsional (T), and elongation (E) modes. The gray filled region denotes the frequency region outside the BG where the modes strain field is spread on the entire phononic pillar.

The finite-size phononic pillar is placed on a substrate that supports the generation of Love-type SAW, enabling interaction with the pillar's resonant modes. The substrate consists of a 90° Z-rotated ST-cut quartz (90STQ), covered with a 4.2 μm thick silica guiding layer. To analyze the interaction between the LSAW and the phononic structure, we performed transmission simulations involving a single row of phononic pillars (**Fig. 3.3(a)**). Using FE analysis, we simulated a unit cell along the y-axis with periodic boundary conditions to represent an infinitely repeated structure. Perfectly matched layers (PMLs) were applied at the substrate boundaries (**Fig. 3.3(a)**) to suppress reflections of both bulk and guided waves. The LSAW excitation was achieved by applying a voltage across surface boundaries acting as interdigital transducer (IDT) electrodes, placed between the quartz substrate and the silica film. The resulting transmission spectrum, shown in **Fig. 3.3(b)**, reveals two pronounced dips in the amplitude of the total displacement field at approximately 244 MHz and 250 MHz, corresponding to attenuation levels of 54% and 90%, respectively. **Figures 3.3(c)** and **(d)** illustrate the displacement field amplitudes within the phononic pillar and the u_y component in the substrate, which is the dominant displacement component for LSAW. These transmission dips are attributed to the excitation of localized resonant modes, specifically the flexural (F) and torsional (T) modes, within the free silica layer at the top of the pillar, where the mechanical energy is highly confined. The displacement amplitude decays rapidly through the upper silica/tungsten layers, with nearly no vibration transmitted to the lower layers of the pillar. This confinement is enabled by the presence of the phononic BG, which inhibits wave propagation into the pillar base.

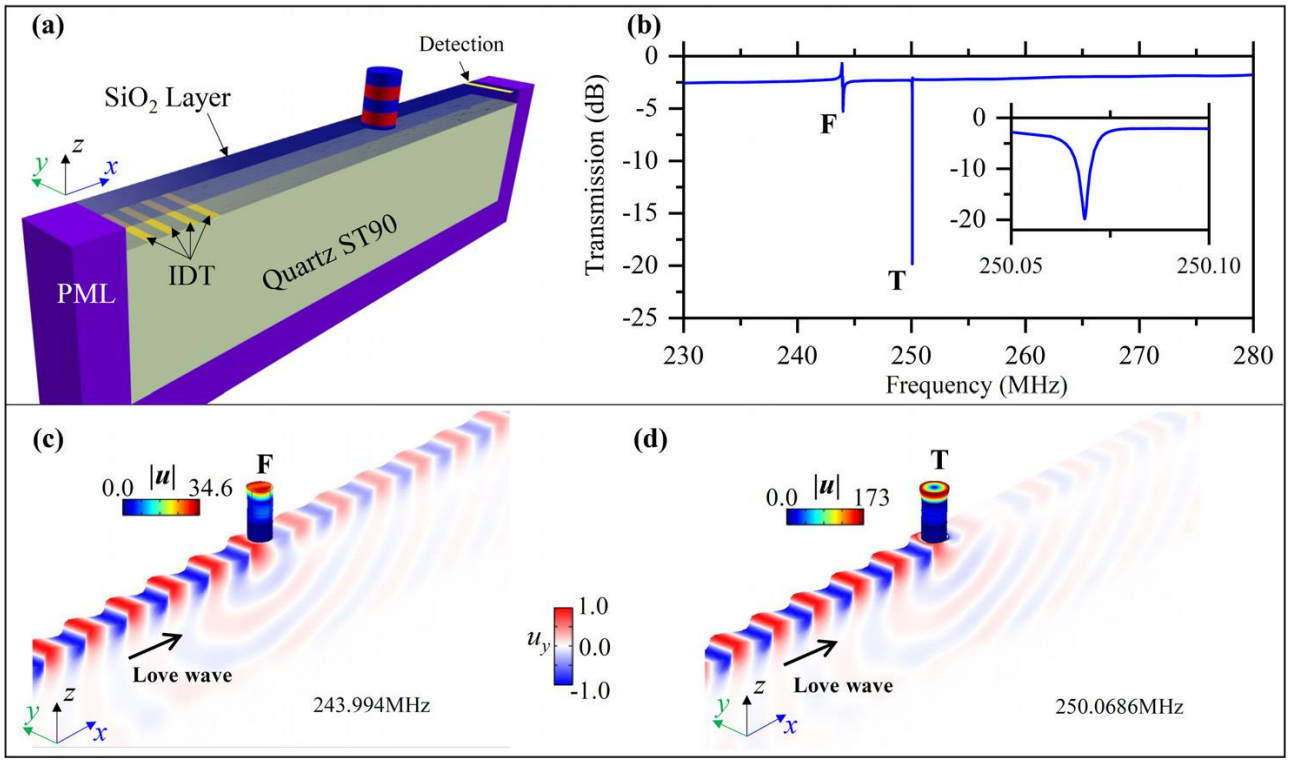

Fig. 3.3. (a) Schematic representation of the unit cell used for FE simulation of the system. (b) LSAW transmission result: normalized transmitted signal (in dB); the F and T dips correspond to the flexural and the torsional modes, respectively. The inset shows an enlargement of dip T. (c), (d) Displacement field amplitudes for modes F (c) and T (d) at their excitation frequencies as well as the displacement component $\underline{u}_y$ in the substrate[55].

The torsional mode exhibits the highest mechanical quality factor (QF), reaching 8.3×10^4, which makes it a highly promising candidate for enhanced sensing applications. We investigated the mass sensitivity of the torsional mode (T) using a simplified theoretical approach. Assuming that the size of each particle is negligible compared to the dimensions of the pillar, we consider a total of N nanoparticles, each with a mass δ_m, uniformly distributed over the pillar surface S, leading to a surface density $\sigma = N/S$. Each nanoparticle is modeled as a rigid mass, and its mechanical stiffness is neglected due to its small size relative to the pillar and the minimal strain it induces in the torsional mode. The binding of these particles to the surface of the phononic micro-pillar locally alters its mechanical properties, resulting in a shift in the resonance frequency. Using perturbation theory, the fractional frequency shift induced by the adsorption of N particles can be estimated by the following expression[152],

$$\frac{\delta\omega}{\omega_0} = -\delta_m\sigma\frac{\int_S \|\boldsymbol{u}\|^2 ds}{2\int_V \rho\|\boldsymbol{u}\|^2 dv} \tag{3.1}$$

For the calculations, we consider as an example a typical viral particle with a mass $\delta_m = 1.15$ fg. **Figure 3.4(b)** presents the frequency shift of the torsional (T) mode as a function of the number of particles N, obtained using both perturbation theory and a numerical method based on FE modeling. Both approaches yield nearly identical results up to approximately 3×10^4 particles, where the frequency shift reaches about –15 MHz. Beyond this point, however, the two results begin to diverge significantly. The linear expression (Eq. 3.1), derived from first-order perturbation theory, becomes invalid for $N > 3\times10^4$, indicating the need to incorporate higher-order perturbative terms to accurately match the numerically computed frequency shifts.

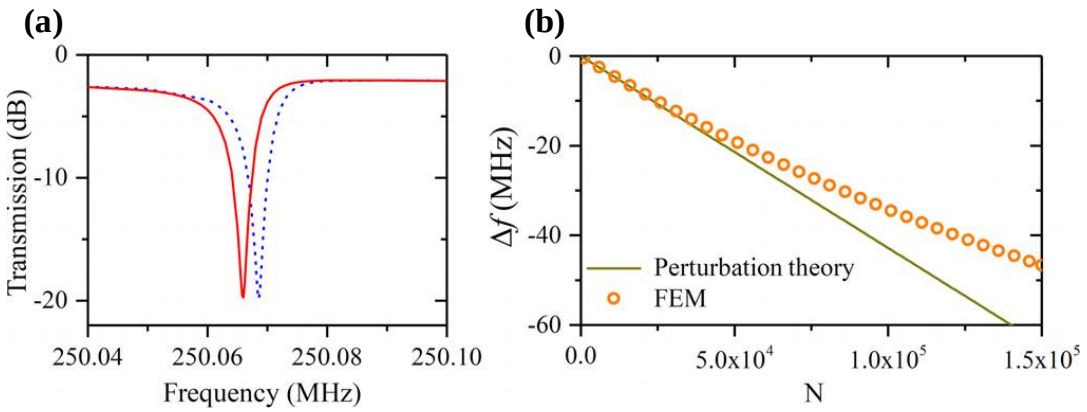

Fig. 3.4. (a) Transmission calculation for the case without (blue dashed line) and with mass perturbation (red solid line). (b) Frequency shift of the tortional mode T as a function of the particle number N. Comparison between the perturbation theory (solid line) and numerical simulation based on FEM (circles)[55].

This theoretical study opens a promising avenue for the development of high-performance SAW-based biosensors by harnessing the wave control capabilities of PnC and metamaterials. In practical implementations, one can envision functionalizing the upper silica layer of the phononic pillar with bioreceptors to enable molecular binding. Although the effect of the chemical layer associated with the bioreceptors is not explicitly considered in this study, it can be approximated as a uniform mass distribution along the pillar's surface, which would similarly induce a shift in the resonant frequency. Loss mechanisms also play a critical role and must be accounted for through evaluation of the signal-to-noise ratio (SNR) and the mechanical quality factor. In this context, the combined pillar and bioreceptor layer can be treated as the unperturbed system. Molecular binding events can then be monitored in real time by tracking shifts in the resonant frequencies of the phononic crystal modes within the SAW transmission spectrum.

3.3 Pillared metamaterial for enhanced SAW sensing

Given the fabrication challenges of complex multilayered phononic pillars at the microscale, we first investigate a simpler system: a lattice of homogeneous micro-pillars integrated onto a SAW device[56]. The goal is to assess how metamaterials can enhance SAW sensor sensitivity, with a particular focus on the local resonant modes of the pillars that interact with SAW. The system consists of a Love-wave platform using an SU-8 guiding layer on a Y+36° cut lithium niobate substrate, onto which a square lattice of SU-8 pillars is deposited. We computed the band structure of this pillar lattice on the SU-8 layer (**Fig. 3.5(a)**), indicating the sound line separating SAW from bulk waves. Since both Rayleigh and Love waves can propagate in this platform, we focus exclusively on Love waves by identifying bands dominated by the shear-horizontal (SH) displacement component u_y (gray-blue scale in **Fig. 3.5(a)**). The blue-colored modes correspond then to Love-type waves. We also analyzed the displacement field amplitudes at the X point of the Brillouin zone to identify pillar resonances coupled with the Love wave. As expected, clear coupling is observed between the Love wave and the flexural mode F_2 at 35.4 MHz, as well as the torsional mode T at 72.2 MHz. In contrast, the flexural mode F_1, vibrating along the *x*-direction, does not couple with the Love wave.

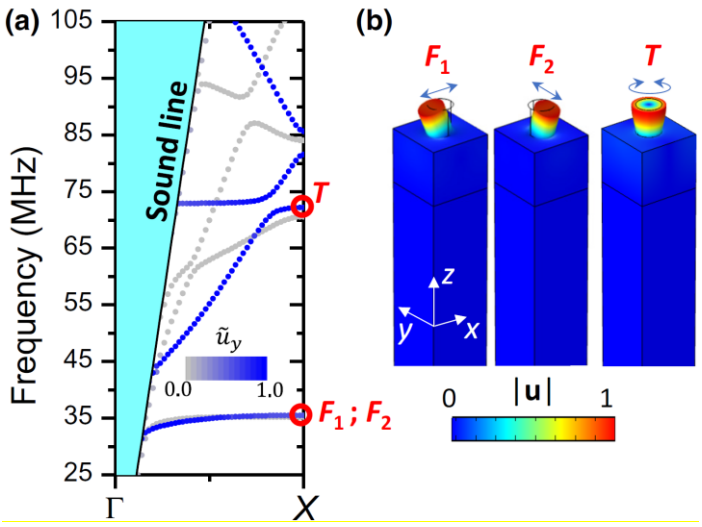

Fig. 3.5. (a) Band structure for the lattice of pillars on the SU-8/LiNbO3 substrate. Gray-blue scale indicates the modes that have a dominant displacement component u_y amplitude. (b) Displacement fields of the resonant flexural and torsional modes at the X point of the Brillouin zone[56].

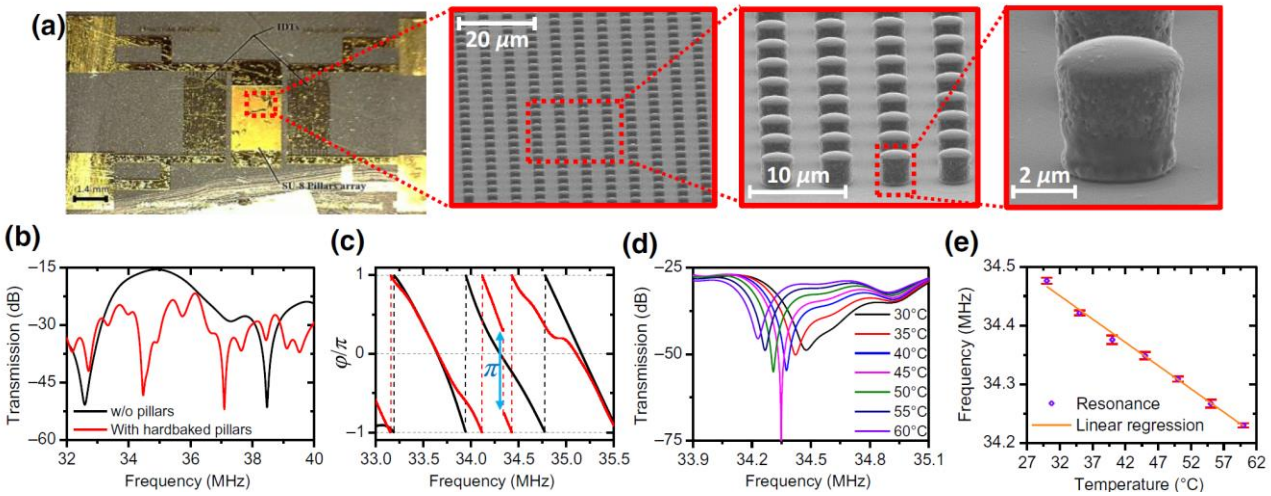

Fig. 3.6. (a) Image of the device (left panel) and SEM images (close-up views) of pillar-based metamaterial at different scales. (b) Experimental frequency spectrum of Love-wave transmission without pillars (black curve) and with SU8 pillars (red curve). (c) Phase of the transmitted signals as a function of the frequency for the sample without pillars (black curve) and with pillars (red curve). (d) Evolution of the resonance dip as a function of the temperature. (e) Linear dependency of the resonance frequency with temperature[56].

The fabrication and full characterization of the device were carried out with detailed procedures provided in Ref.[56]. **Figure 3.6(a)** presents the fabricated device along with SEM images showing the lattice of pillars. The frequency response spectra of the device are shown in **Fig. 3.6(b)** for two cases: without pillars and with pillars. In the spectrum of the sample with pillars (red curve), an additional dip appears in the central lobe at 34.47 MHz, corresponding to the excitation of the flexural vibration mode of the pillars. The phase measurement of the transmitted signal (S21 parameter), displayed in **Fig. 3.6(c)**, reveals a π phase jump at 34.47 MHz, which confirms the resonant behavior of the pillars at this frequency.

The sensing performance of the device was first evaluated for temperature variation detection. The measurements indicate that the resonance frequency of the pillars decreases with increasing temperature, as shown in **Fig. 3.6(d)** and **(e)**. The temperature sensitivity of the device was determined to be 229.23 ppm/K (from **Fig. 3.6(e)**), which at the time of publication [Ref. [56]], represents the highest value reported compared to

conventional Rayleigh- and Love-wave-based sensors. We also investigated the device's performance in detecting the concentration of polystyrene microbeads in aqueous solution. Several micro-droplets (7μL each) of polystyrene bead suspensions, with a mean particle diameter of 1 μm, were prepared to ensure full coverage of the surface area occupied by the pillar array (**Fig. 3.7(a)**). The resulting frequency shifts as a function of microbead concentration are shown in **Fig. 3.7(b)**, where a clear downshift in resonance frequency is observed with increasing particle concentration. From these data, the mass sensitivity of the device was calculated to be 220.3 $m^2 \cdot kg^{-1}$. For the chosen guiding-layer thickness-to-wavelength ratio $d/\lambda \approx 0.07$, this sensitivity is approximately one order of magnitude higher than that of previously reported Love-wave-based sensors employing only interdigitated transducers (Ref.[153]). This demonstration suggests a promising route for the development of SAW-based sensing platforms with enhanced sensitivity enabled by surface-engineered metamaterial structures.

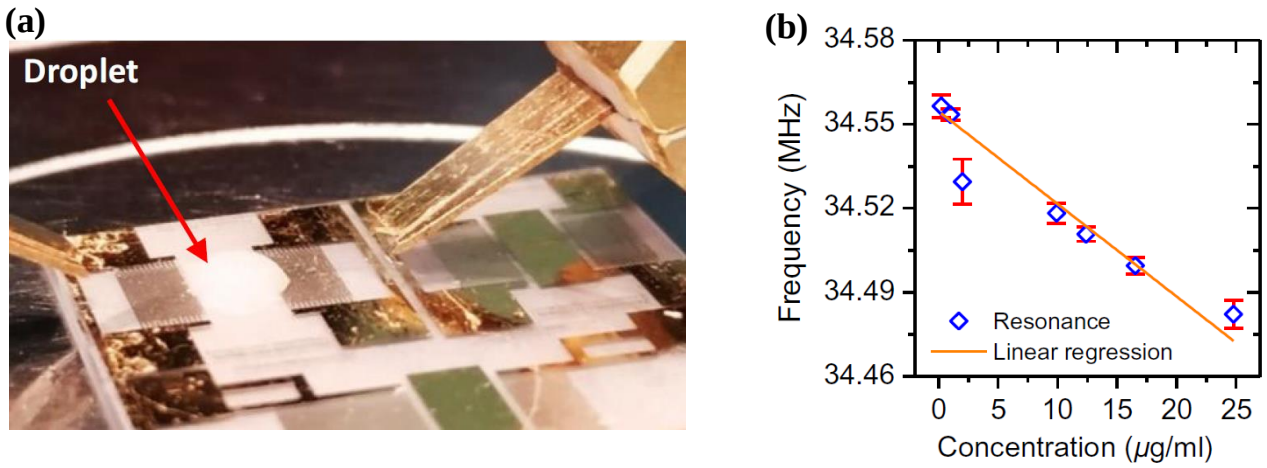

Fig. 3.7. (a) Image of the device with a droplet with microbeads solution deposited on top of the pillars array. (b) The frequency shift of the resonance mode of the pillar as function of concentration of polystyrene microbeads in the microdroplet.

Chapter 4: Non-reciprocal elastic metamaterials

A fundamental concept in wave physics, particularly acoustics, is the principle of reciprocity, which states that the transmission response between two spatial locations is identical in both directions. Over the past decade, increasing research has focused on breaking reciprocity to enable unidirectional wave propagation. Nonreciprocal acoustic devices that allow one-way sound transmission are highly sought for applications such as unidirectional sound barrier, advanced medical ultrasound, and SAW-based communication systems[154]. In this chapter, we first review key literature on acoustic reciprocity breaking, then introduce the concept of space-time phononic crystals, with emphasis on one-dimensional configurations and their dispersive and nonreciprocal properties. Finally, we present a compact nonreciprocal system and experimentally demonstrate unidirectional flexural wave propagation.

4.1 Breaking reciprocity in acoustics

Breaking reciprocity can be achieved by introducing nonlinearity, loss, or a deliberate bias in the physical properties of the propagation medium in space and time. These mechanisms must be carefully engineered into the medium. Various acoustic platforms have been developed to explore acoustic nonreciprocity, exhibiting distinct wave behaviors depending on the direction of propagation. Early demonstrations of acoustic nonreciprocity successfully employed a combination of nonlinear media with PnCs[155,156]. Later approaches used geometrical design strategies to induce asymmetric wave dispersion; however, such systems do not truly break reciprocity but instead affect wave packet paths and mode shapes[157,158]. A particularly intriguing approach to breaking reciprocity involves the space-time modulation (STM) of a medium's intrinsic properties to disrupt time-reversal symmetry. First proposed in 1959 in the context of photonics and electrical circuits, this concept involves harmonic modulation of permittivity, permeability, or impedance in both space and time, creating unidirectional BG[159,160]. In such a medium, intrinsic properties appear to change and move spatially at a certain velocity, leading to different dispersion relations for waves traveling in opposite directions along the same path. This method of breaking time-reversal symmetry, and thus reciprocity, was largely overlooked for decades until recent technological advances in fabrication and characterization reignited interest in STM systems[161–164]. Inspired by developments in photonics, several STM-based concepts have been translated to acoustics[165–168] and elastodynamics[169–172]. The following section presents a summary of the studies we have conducted in this rapidly evolving field.

4.2 Non-reciprocal phononic crystal

The general case for acoustic wave propagation in a fluid medium whose effective properties (density and compressibility) vary both in space and time, can be studied using the governing equation:

$$\begin{aligned} \boldsymbol{\nabla} p &= -\rho(\boldsymbol{r}, t)\frac{\partial \boldsymbol{v}}{\partial t} \\ \boldsymbol{\nabla}.\boldsymbol{v} &= -K_e(\boldsymbol{r}, t)\frac{\partial p}{\partial t} \end{aligned} \tag{4.1}$$

where p is the pressure, $\boldsymbol{v}$ is the particle velocity field, and $\rho(\boldsymbol{r},t)$ and $K_e(\boldsymbol{r},t)$ are the space and time dependent density and compressibility of the medium, respectively (**Fig. 4.1(a)**).

For instance, in one-dimensional space-time PnC, one can consider the modulation of the density in a coupled manner : $\rho(x,t)=\rho_0\left(1+\alpha.cos(\omega_m t-k_m x)\right)$ where ρ_0 is the constate mean density of the medium, α is the modulation rate, $k_m=2\pi/\lambda_m$ and $\omega_m=2\pi/T_m$ where λ_m and T_m are the space and time periods of the modulation, respectively (**Fig. 4.1(b)**).

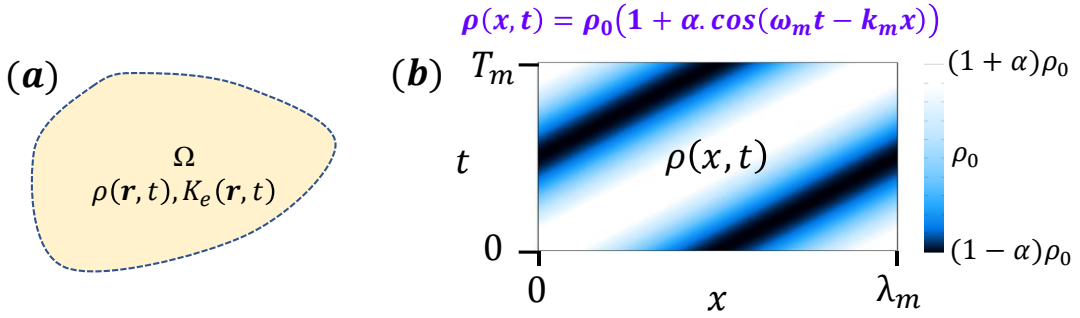

Fig. 4.1. (a) General case of a propagating domain where compressibility and density are both dependent on space and time variables $\boldsymbol{r}$ and t respectively. (b) an example of density that is modulated both in space and time, a unit cell of the space-time PnC: α is the modulation rate, $k_m=2\pi/\lambda_m$ and $\omega_m=2\pi/T_m$ where λ_m and T_m are the space and time periods of the modulation, respectively.

Starting from this example, the solution for equation (4.1) can be described in plane waves expansion,

$$p(x,t)=\sum_{n=-\infty}^{n=+\infty} p_n exp\left(i\left(\omega t-kx+n(\omega_m t-k_m x)\right)\right)$$
$$v(x,t)=\sum_{n=-\infty}^{n=+\infty} v_n exp\left(i\left(\omega t-kx+n(\omega_m t-k_m x)\right)\right) \quad (4.2)$$

Inserting these equations into Eq.4.1, and by choosing a sufficient number of decompositions, one can construct an eigenfrequency problem to solve in order to get the band structure of the 1D space-time phononic crystal. **Figure 4.2** displays the results for the cases without time modulation ($\omega_m=0$) (**Fig. 4.2(a)**) which corresponds to the classical PnC, and the case with a time modulation ($\omega_m\neq 0$) (**Fig. 4.2(b)**). Without time modulation, two BGs (green filled regions denoted BG1 and BG2 in **Fig. 4.2(a)**) are open for both opposite direction of propagations k^+ (positive *x* direction) and k^- (negative *x* direction). However, in the case of time modulation, the frequency bands in k^+ direction shift to higher frequencies while those for k^- direction shift to lower frequencies, resulting in shifted BGs for opposite direction of propagation (shaded pink and orange regions in the band structure of **Fig. 4.2 (b)**). Consequently, if we consider a finite number of units of the space time modulated PnC (**Fig. 4.2 (c)**) and conduct a wave transmission analysis, the wave fields shown that a pressure wave at the normalized frequency Ω=0.41 will propagate in the k^+ direction while it will get almost completely reflected in the k^- direction (left panels in **Fig. 4.2 (c)**) because of the existence of bandgap $BG1^-$ for the frequency Ω=0.41 (**Fig. 4.2 (b)**). However, the opposite situation happens for an incident wave at Ω=0.61 where the wave is transmitted through the space-time PnC in the k^- direction while it is almost totally reflected in the k^+ direction because of the existance of $BG1^+$ (**Fig. 4.2 (b)**).

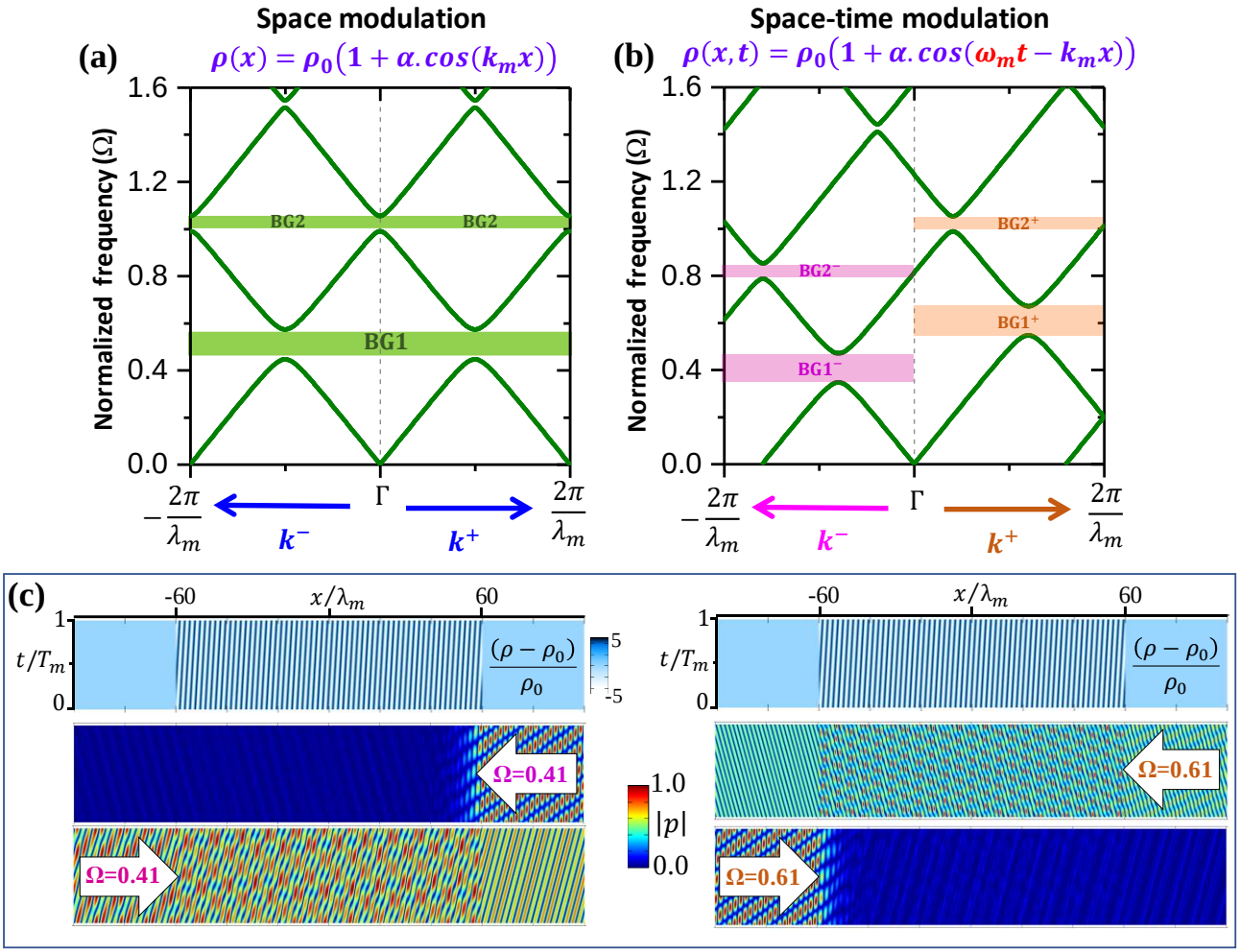

Fig. 4.2. (a) the band structure calculation for the case of 1D PnC where the density is only modulated in space along the *x* direction corresponding to the acoustic wave propagation direction. (b) Band structure for the space-time PnC where the density is modulated both in space and time following the equation: $\rho(x,t) = \rho_0(1 + \alpha\cos(\omega_m t - k_m x))$. (c) Transmission through finite number of unit cells of the space-time PnC. The upper panels correspond to color maps showing how the density changes over time and space. 120 periods were chosen in space. The lower panels display pressure field amplitude for acoustic waves propagating in opposite directions at different normalized frequencies Ω=0.41 (left) and Ω=0.61 (right).

4.3 Nonreciprocal Sound Propagation via Cascaded Time-Modulated Slab Resonators

In acoustics, while it is locally feasible to dynamically modulate the effective density of air[173], achieving precise harmonic modulation in both space and time over multiple periods remains highly challenging. In contrast, nonreciprocity based on space-time modulation is more readily attainable in elastodynamics, where the effective stiffness of the material can be modulated[170–172]. This typically involves integrating coils or piezoelectric elements connected to electrical circuits to induce effective negative stiffness, a process that adds complexity, especially in synchronizing the modulations. As a result, such nonreciprocal devices often become bulky and less practical for many real-world applications. A more practical and compact alternative for achieving acoustic nonreciprocity is the use of cascaded, coupled Fabry–Pérot-based slabs[174]. In addition to their reduced footprint, these structures offer high transmission efficiency at Fabry–Pérot resonances and the possibility of enabling unidirectional wave propagation through mode conversion. This approach provides

greater control over nonreciprocal behavior, making it a promising candidate for future acoustic device integration.

The configuration of the compact cascaded time-modulated slabs is illustrated in **Fig. 4.3(a)**. It consists of two acoustic media (slabs), each with time-varying density profiles, denoted as $\rho_1(t)$ and $\rho_2(t)$, modulated with a relative phase shift $\Delta\varphi$. The background medium is assumed to be air, with a constant density ρ_0. In practice, such temporal modulations can be implemented, for example, by using piston-like mechanisms driven by rotating elements to induce periodic compressions. When an incident acoustic plane wave of angular frequency ω interacts with this system, the reflected p_r and transmitted p_t fields, as well as the internal fields within and between the slabs, exhibit higher-order harmonics of the form $\omega + n\omega_m$, where ω_m is the modulation frequency and n is an integer. The amplitudes of these harmonic components can be determined using the Transfer Matrix Method (TMM), allowing for a detailed analysis of both reflected and transmitted pressure waves[174].

After optimizing the geometrical and modulation parameters, the system exhibits non-reciprocal acoustic transmission. **Figures 4.3(b)** and **4.3(c)** show the transmission coefficients for both forward and reverse propagation of a monochromatic incident wave. These results compare the TMM predictions (represented as orange segments corresponding to discrete harmonic orders) with finite element (FE) simulations, where the transmission spectra are extracted from time-domain transient responses (blue curves). The close agreement between both approaches confirms the validity of the model. The analysis reveals that the zeroth-order transmitted mode dominates in the negative propagating direction, while it is significantly suppressed in the positive direction, where energy is converted into higher-order modes. **Figure 4.3(d)** further illustrates this unidirectional transmission for the fundamental mode and highlights the system's ability to support broadband acoustic nonreciprocity.

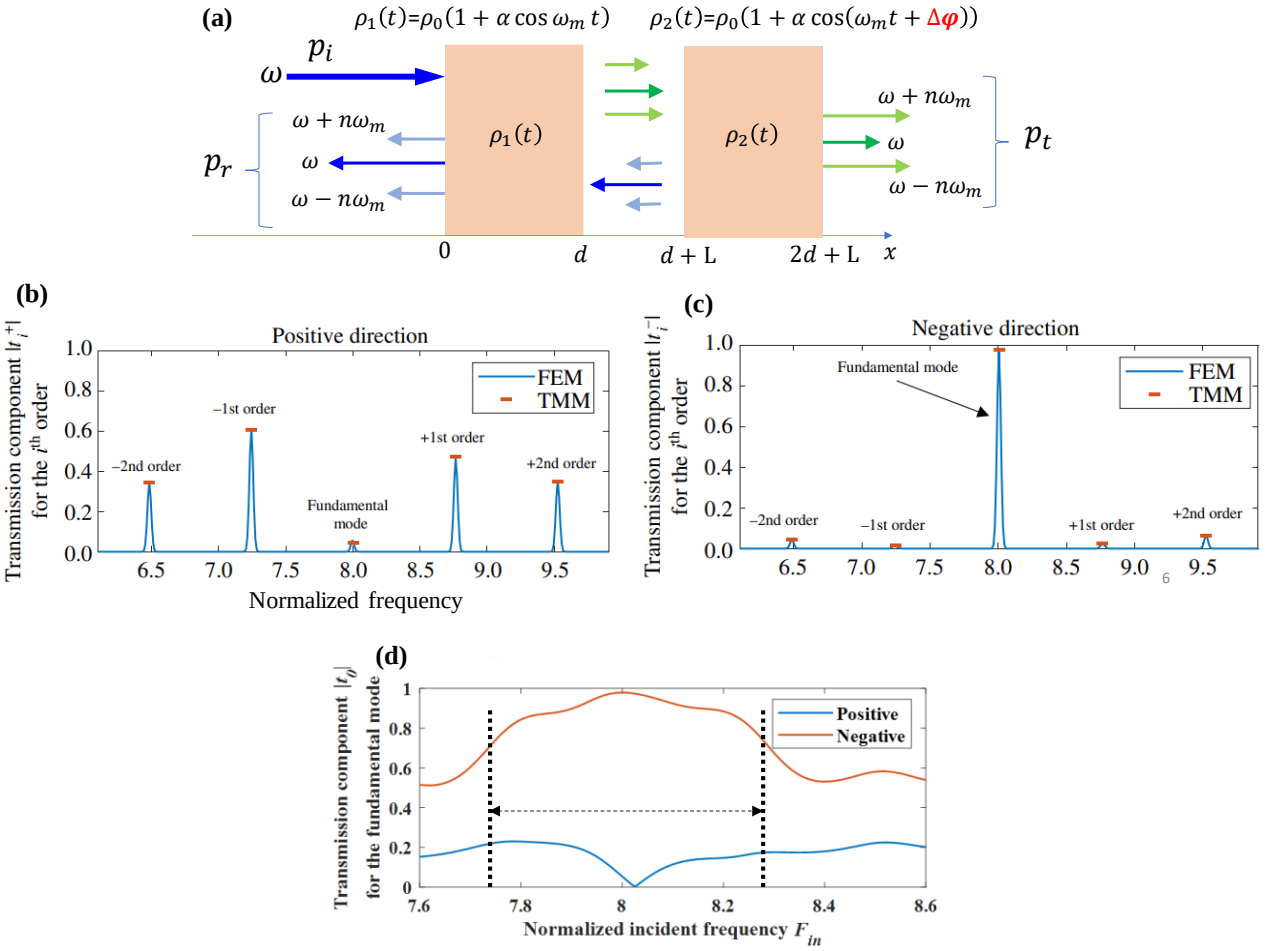

Fig. 4.3. (a) Schematic of a two-cascaded-slab with time-modulated effectives densities with a phase shift in the modulation. High order modes (harmonics) appear in the transmitted and reflected waves due to time modulation. (b), (c) Transmission coefficients for the positive direction (b) and the negative direction (b). (d) Calculated transmission coefficient curve for the fundamental mode (zeroth order) for both directions as a function of the normalized frequency. Black dashed lines and arrows mark the bandwidth for at least 50% transmission rate difference between positive and negative directions of propagation[174].

4.4 Nonreciprocal flexural wave propagation via compact cascaded time-modulated resonators

To realize such a compact device, we focus on flexural wave propagation in a beam, where it is more feasible to modulate the system's effective stiffness. We designed and fabricated a compact, low-frequency nonreciprocal waveguide for flexural waves, using only two time-modulated mechanical resonators[175], as shown in **Fig. 4.4(a)** and **(b)**. These resonators are implemented through a coil–cantilever–magnet assembly, where the effective stiffness can be dynamically tuned by applying an alternating current (AC) (**Fig. 4.4(c)** and **(d)**). Specifically, the magnetic force between a magnet attached to the beam and a coil mounted on a cantilever is varied by modulating the current, thereby altering the resonator's stiffness over time (**Fig. 4.4(d)**). By applying a controlled phase shift between the AC signals driving the two resonators, their stiffness is harmonically modulated in time with a phase offset, introducing a spatiotemporal bias. This bias breaks reciprocity, enabling nonreciprocal transmission of flexural waves through the beam.

For the long-wavelength regime, where the wavelength is much greater than the beam thickness, a theoretical model is built and accurately describes the system's dynamics. The full analytical formulation and validation of this model are detailed in Ref. [175].

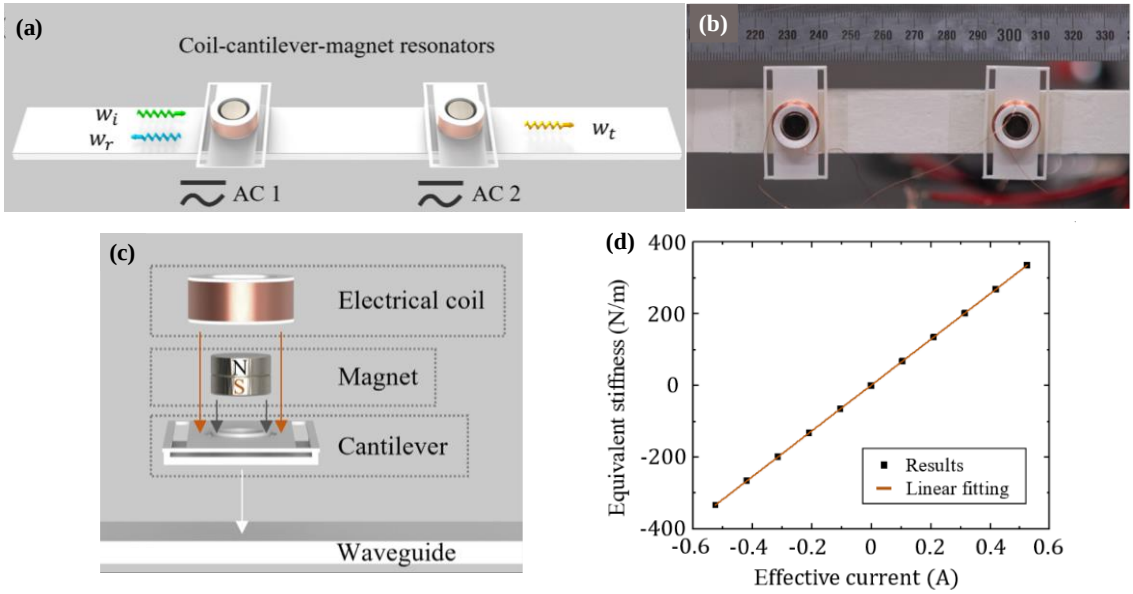

Fig. 4.4. (a) Schematic of the coil-cantilever-magnet cascaded bi-resonator system with temporally modulated effective stiffness through an applied AC in the coil. (b) Image of the fabricated on-beam coil-cantilever-magnet resonator in our experimental setup. (c) Schematic design of the coil-cantilever-magnet resonator system. (d) Effective stiffness measurements of the active resonator as function of the applied current.

The complete experimental setup is shown in **Fig. 4.5(a)**. Measured transmission results for the positive (left-to-right) and negative (right-to-left) directions, presented in **Fig. 4.5(b)**, clearly demonstrate nonreciprocal flexural wave propagation, with reasonable agreement compared to the theoretical predictions in **Fig. 4.5(c)**. The difference in bandwidth between measurement and theory stems from modeling approximations related to the resonators. Error bars reflect the stability and reproducibility of the observed nonreciprocal transmission. Importantly, the entire device has a physical size smaller than one-third of the operating wavelength, illustrating its subwavelength nature. This proof-of-concept offers promising prospects for the development of compact nonreciprocal metamaterials, enabling smart flexural wave control for phononic communication systems, imaging platforms, and devices robust against feedback noise.

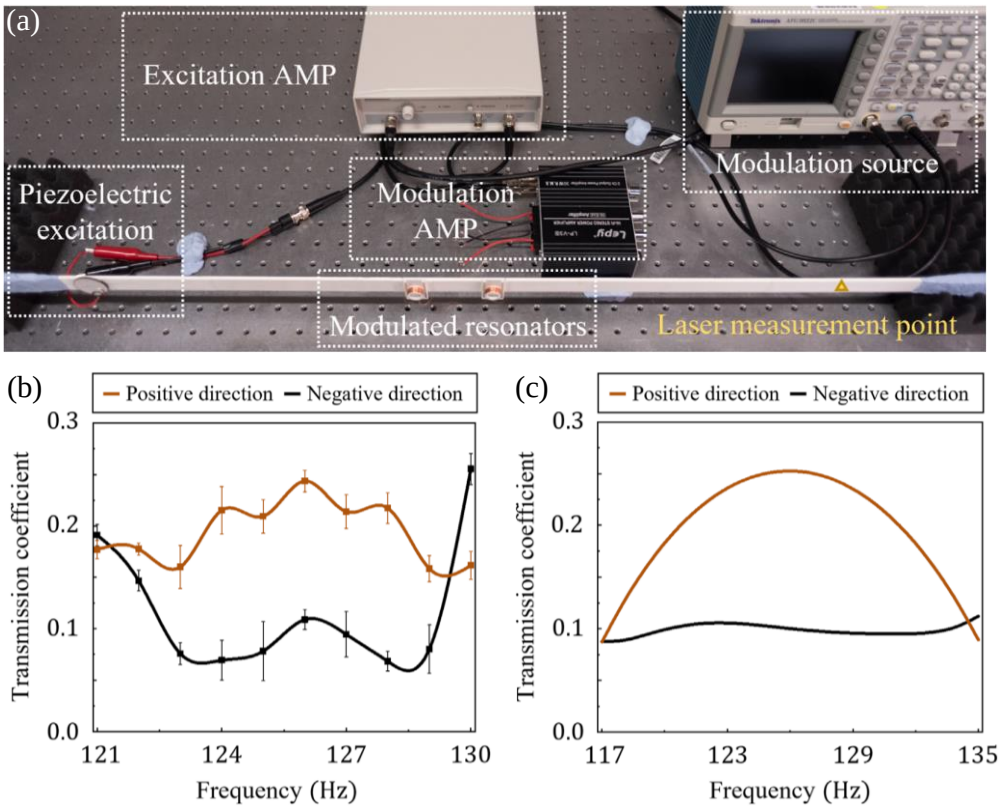

Fig. 4.5. (a) Experimental platform for flexural wave transmission. AMP: amplifier. (b) Results of the transmission measurements from 121 to 130 Hz with error bars, normalized by the results of the bare beam (without resonators). (c) Theoretical transmission coefficient in the frequency domain from the Semi-analytical formulation.

References

1. Tamura, S., Hurley, D. C. & Wolfe, J. P. Acoustic-phonon propagation in superlattices. *Phys. Rev. B* **38**, 1427–1449 (1988).
2. Sigalas, M. M. & Economou, E. N. Elastic and acoustic wave band structure. *J. Sound Vib.* **158**, 377–382 (1992).
3. Sigalas, M. M. & Economou, E. N. Elastic and acoustic wave band structure. *J. Sound Vib.* **158**, 377–382 (1992).
4. Kushwaha, M. S., Halevi, P., Dobrzynski, L. & Djafari-Rouhani, B. Acoustic band structure of periodic elastic composites. *Phys. Rev. Lett.* **71**, 2022–2025 (1993).
5. Liu, Z. *et al.* Locally Resonant Sonic Materials. *Science* **289**, 1734–1736 (2000).
6. Martínez-Sala, R. *et al.* Sound attenuation by sculpture. *Nature* **378**, 241–241 (1995).
7. Mohammadi, S., Eftekhar, A. A., Khelif, A., Hunt, W. D. & Adibi, A. Evidence of large high frequency complete phononic band gaps in silicon phononic crystal plates. *Appl. Phys. Lett.* **92**, 221905 (2008).
8. Meseguer, F. *et al.* Rayleigh-wave attenuation by a semi-infinite two-dimensional elastic-band-gap crystal. *Phys. Rev. B* **59**, 12169–12172 (1999).
9. Khelif, A., Aoubiza, B., Mohammadi, S., Adibi, A. & Laude, V. Complete band gaps in two-dimensional phononic crystal slabs. *Phys. Rev. E* **74**, 046610 (2006).
10. Maldovan, M. & Thomas, E. L. Simultaneous complete elastic and electromagnetic band gaps in periodic structures. *Appl. Phys. B* **83**, 595–600 (2006).
11. Eichenfield, M., Chan, J., Camacho, R. M., Vahala, K. J. & Painter, O. Optomechanical crystals. *Nature* **462**, 78–82 (2009).
12. Eichenfield, M., Chan, J., Safavi-Naeini, A. H., Vahala, K. J. & Painter, O. Modeling dispersive coupling and losses of localized optical and mechanical modes in optomechanical crystals. *Opt. Express* **17**, 20078–20098 (2009).
13. Safavi-Naeini, A. H. *et al.* Electromagnetically induced transparency and slow light with optomechanics. *Nature* **472**, 69–73 (2011).
14. Chan, J. *et al.* Laser cooling of a nanomechanical oscillator into its quantum ground state. *Nature* **478**, 89–92 (2011).
15. Safavi-Naeini, A. H. *et al.* Two-Dimensional Phononic-Photonic Band Gap Optomechanical Crystal Cavity. *Phys. Rev. Lett.* **112**, 153603 (2014).
16. Gomis-Bresco, J. *et al.* A one-dimensional optomechanical crystal with a complete phononic band gap. *Nat. Commun.* **5**, 4452 (2014).
17. Oudich, M. *et al.* Optomechanic interaction in a corrugated phoxonic nanobeam cavity. *Phys. Rev. B* **89**, 245122 (2014).
18. Chan, J., Safavi-Naeini, A. H., Hill, J. T., Meenehan, S. & Painter, O. Optimized optomechanical crystal cavity with acoustic radiation shield. *Appl. Phys. Lett.* **101**, 081115 (2012).
19. Fang, K., Matheny, M. H., Luan, X. & Painter, O. Optical transduction and routing of microwave phonons in cavity-optomechanical circuits. *Nat. Photonics* **10**, 489–496 (2016).
20. Gil-Santos, E. *et al.* Optomechanical detection of vibration modes of a single bacterium. *Nat. Nanotechnol.* **15**, 469–474 (2020).
21. Yu, W., Jiang, W. C., Lin, Q. & Lu, T. Cavity optomechanical spring sensing of single molecules. *Nat. Commun.* **7**, 12311 (2016).
22. Navarro-Urrios, D. *et al.* Optomechanical crystals for spatial sensing of submicron sized particles. *Sci. Rep.* **11**, 7829 (2021).
23. Riedinger, R. *et al.* Remote quantum entanglement between two micromechanical oscillators. *Nature* **556**, 473–477 (2018).
24. Wang, Y.-T., Luan, P.-G. & Zhang, S. Coriolis force induced topological order for classical mechanical vibrations. *New J. Phys.* **17**, 073031 (2015).
25. Nash, L. M. *et al.* Topological mechanics of gyroscopic metamaterials. *Proc. Natl. Acad. Sci. U. S. A.* **112**, 14495–14500 (2015).
26. Wang, P., Lu, L. & Bertoldi, K. Topological Phononic Crystals with One-Way Elastic Edge Waves. *Phys. Rev. Lett.* **115**, 104302 (2015).
27. Mousavi, S. H., Khanikaev, A. B. & Wang, Z. Topologically protected elastic waves in phononic metamaterials. *Nat. Commun.* **6**, 8682 (2015).
28. Süsstrunk, R. & Huber, S. D. Observation of phononic helical edge states in a mechanical topological insulator. *Science* **349**, 47–50 (2015).

29. Miniaci, M., Pal, R. K., Morvan, B. & Ruzzene, M. Experimental Observation of Topologically Protected Helical Edge Modes in Patterned Elastic Plates. *Phys. Rev. X* **8**, 031074 (2018).
30. Zhu, H., Liu, T.-W. & Semperlotti, F. Design and experimental observation of valley-Hall edge states in diatomic-graphene-like elastic waveguides. *Phys. Rev. B* **97**, 174301 (2018).
31. Yan, M. *et al.* On-chip valley topological materials for elastic wave manipulation. *Nat. Mater.* **17**, 993–998 (2018).
32. Darabi, A., Collet, M. & Leamy, M. J. Experimental realization of a reconfigurable electroacoustic topological insulator. *Proc. Natl. Acad. Sci.* **117**, 16138–16142 (2020).
33. Zhang, Q., Chen, Y., Zhang, K. & Hu, G. Dirac degeneracy and elastic topological valley modes induced by local resonant states. *Phys. Rev. B* **101**, 014101 (2020).
34. Nash, L. M. *et al.* Topological mechanics of gyroscopic metamaterials. *Proc. Natl. Acad. Sci.* **112**, 14495–14500 (2015).
35. Yang, Z. *et al.* Topological Acoustics. *Phys. Rev. Lett.* **114**, 114301 (2015).
36. Xiao, M., Chen, W.-J., He, W.-Y. & Chan, C. T. Synthetic gauge flux and Weyl points in acoustic systems. *Nat. Phys.* **11**, 920–924 (2015).
37. Li, F., Huang, X., Lu, J., Ma, J. & Liu, Z. Weyl points and Fermi arcs in a chiral phononic crystal. *Nat. Phys.* **14**, 30–34 (2018).
38. Rosa, M. I. N., Pal, R. K., Arruda, J. R. F. & Ruzzene, M. Edge States and Topological Pumping in Spatially Modulated Elastic Lattices. *Phys. Rev. Lett.* **123**, 034301 (2019).
39. Yu, S.-Y. *et al.* Elastic pseudospin transport for integratable topological phononic circuits. *Nat. Commun.* **9**, 3072 (2018).
40. Cha, J., Kim, K. W. & Daraio, C. Experimental realization of on-chip topological nanoelectromechanical metamaterials. *Nature* **564**, 229–233 (2018).
41. Chaunsali, R., Chen, C.-W. & Yang, J. Experimental demonstration of topological waveguiding in elastic plates with local resonators. *New J. Phys.* **20**, 113036 (2018).
42. Zhang, Z.-D. *et al.* Topological Surface Acoustic Waves. *Phys. Rev. Appl.* **16**, 044008 (2021).
43. Mitchell, N. P., Nash, L. M. & Irvine, W. T. M. Tunable band topology in gyroscopic lattices. *Phys. Rev. B* **98**, 174301 (2018).
44. Serra-Garcia, M. *et al.* Observation of a phononic quadrupole topological insulator. *Nature* **555**, 342–345 (2018).
45. Fan, H., Xia, B., Tong, L., Zheng, S. & Yu, D. Elastic Higher-Order Topological Insulator with Topologically Protected Corner States. *Phys. Rev. Lett.* **122**, 204301 (2019).
46. Xie, B. *et al.* Higher-order band topology. *Nat. Rev. Phys.* **3**, 520–532 (2021).
47. Horowitz, S. B., Sheplak, M., Cattafesta, L. N. & Nishida, T. A MEMS acoustic energy harvester. *J. Micromechanics Microengineering* **16**, S174 (2006).
48. Noh, S., Lee, H. & Choi, B. A study on the acoustic energy harvesting with Helmholtz resonator and piezoelectric cantilevers. *Int. J. Precis. Eng. Manuf.* **14**, 1629–1635 (2013).
49. Li, B., You, J. H. & Kim, Y.-J. Low frequency acoustic energy harvesting using PZT piezoelectric plates in a straight tube resonator. *Smart Mater. Struct.* **22**, 055013 (2013).
50. Li, B., Laviage, A. J., You, J. H. & Kim, Y.-J. Harvesting low-frequency acoustic energy using quarter-wavelength straight-tube acoustic resonator. *Appl. Acoust.* **74**, 1271–1278 (2013).
51. Lucklum, R. & Li, J. Phononic crystals for liquid sensor applications. *Meas. Sci. Technol.* **20**, 124014 (2009).
52. Lucklum, R., Ke, M. & Zubtsov, M. Two-dimensional phononic crystal sensor based on a cavity mode. *Sens. Actuators B Chem.* **171–172**, 271–277 (2012).
53. Oseev, A., Zubtsov, M. & Lucklum, R. Gasoline properties determination with phononic crystal cavity sensor. *Sens. Actuators B Chem.* **189**, 208–212 (2013).
54. Pennec, Y., Jin, Y. & Djafari-Rouhani, B. Chapter Two - Phononic and photonic crystals for sensing applications. in *Advances in Applied Mechanics* (ed. Hussein, M. I.) vol. 52 105–145 (Elsevier, 2019).
55. Bonhomme, J. *et al.* Love waves dispersion by phononic pillars for nano-particle mass sensing. *Appl. Phys. Lett.* **114**, 013501 (2019).
56. Bonhomme, J. *et al.* Micropillared Surface to Enhance the Sensitivity of a Love-Wave Sensor. *Phys. Rev. Appl.* **17**, 064024 (2022).
57. Song, J. *et al.* Processing bulk natural wood into a high-performance structural material. *Nature* **554**, 224–228 (2018).
58. Meyers, M. A., Chen, P.-Y., Lin, A. Y.-M. & Seki, Y. Biological materials: Structure and mechanical properties. *Prog. Mater. Sci.* **53**, 1–206 (2008).

59. Zheng, X. *et al.* Ultralight, ultrastiff mechanical metamaterials. *Science* **344**, 1373–1377 (2014).
60. Zheng, X. *et al.* Multiscale metallic metamaterials. *Nat. Mater.* **15**, 1100–1106 (2016).
61. Hedayati, R., Leeflang, A. M. & Zadpoor, A. A. Additively manufactured metallic pentamode metamaterials. *Appl. Phys. Lett.* **110**, 091905 (2017).
62. Taniker, S. & Yilmaz, C. Design, analysis and experimental investigation of three-dimensional structures with inertial amplification induced vibration stop bands. *Int. J. Solids Struct.* **72**, 88–97 (2015).
63. Matlack, K. H., Bauhofer, A., Krödel, S., Palermo, A. & Daraio, C. Composite 3D-printed metastructures for low-frequency and broadband vibration absorption. *Proc. Natl. Acad. Sci.* **113**, 8386–8390 (2016).
64. Fei, X., Jin, L., Zhang, X., Li, X. & Lu, M. Three-dimensional anti-chiral auxetic metamaterial with tunable phononic bandgap. *Appl. Phys. Lett.* **116**, 021902 (2020).
65. Muhammad & Lim, C. W. Phononic metastructures with ultrawide low frequency three-dimensional bandgaps as broadband low frequency filter. *Sci. Rep.* **11**, 7137 (2021).
66. Warmuth, F., Wormser, M. & Körner, C. Single phase 3D phononic band gap material. *Sci. Rep.* **7**, 3843 (2017).
67. Gerard, N. J. *et al.* Three-Dimensional Trampolinelike Behavior in an Ultralight Elastic Metamaterial. *Phys. Rev. Appl.* **16**, 024015 (2021).
68. Chen, Z. *et al.* 3D printing of ceramics: A review. *J. Eur. Ceram. Soc.* **39**, 661–687 (2019).
69. Chen, D. & Zheng, X. Multi-material Additive Manufacturing of Metamaterials with Giant, Tailorable Negative Poisson's Ratios. *Sci. Rep.* **8**, 9139 (2018).
70. Wang, P., Shim, J. & Bertoldi, K. Effects of geometric and material nonlinearities on tunable band gaps and low-frequency directionality of phononic crystals. *Phys. Rev. B* **88**, 014304 (2013).
71. Wang, P., Casadei, F., Shan, S., Weaver, J. C. & Bertoldi, K. Harnessing Buckling to Design Tunable Locally Resonant Acoustic Metamaterials. *Phys. Rev. Lett.* **113**, 014301 (2014).
72. Wang, Z., Zhang, Q., Zhang, K. & Hu, G. Tunable Digital Metamaterial for Broadband Vibration Isolation at Low Frequency. *Adv. Mater.* **28**, 9857–9861 (2016).
73. Gliozzi, A. S. *et al.* Tunable photo-responsive elastic metamaterials. *Nat. Commun.* **11**, 2576 (2020).
74. Yeh, J.-Y. Control analysis of the tunable phononic crystal with electrorheological material. *Phys. B Condens. Matter* **400**, 137–144 (2007).
75. Cha, J. & Daraio, C. Electrical tuning of elastic wave propagation in nanomechanical lattices at MHz frequencies. *Nat. Nanotechnol.* **13**, 1016–1020 (2018).
76. Bergamini, A. *et al.* Phononic Crystal with Adaptive Connectivity. *Adv. Mater.* **26**, 1343–1347 (2014).
77. Chen, Y. Y., Hu, G. K. & Huang, G. L. An adaptive metamaterial beam with hybrid shunting circuits for extremely broadband control of flexural waves. *Smart Mater. Struct.* **25**, 105036 (2016).
78. Zhu, R. *et al.* Experimental study of an adaptive elastic metamaterial controlled by electric circuits. *Appl. Phys. Lett.* **108**, 011905 (2016).
79. Robillard, J.-F. *et al.* Tunable magnetoelastic phononic crystals. *Appl. Phys. Lett.* **95**, 124104 (2009).
80. Pierce, C. D. *et al.* Adaptive elastic metastructures from magneto-active elastomers. *Smart Mater. Struct.* **29**, 065004 (2020).
81. Huang, Z.-G. & Wu, T.-T. Temperature effect on the bandgaps of surface and bulk acoustic waves in two-dimensional phononic crystals. *IEEE Trans. Ultrason. Ferroelectr. Freq. Control* **52**, 365–370 (2005).
82. Chuang, K.-C., Lv, X.-F. & Wang, D.-F. A tunable elastic metamaterial beam with flat-curved shape memory alloy resonators. *Appl. Phys. Lett.* **114**, 051903 (2019).
83. Deng, Y. *et al.* Observation of Degenerate Zero-Energy Topological States at Disclinations in an Acoustic Lattice. *Phys. Rev. Lett.* **128**, 174301 (2022).
84. Schneider, K. *et al.* Optomechanics with one-dimensional gallium phosphide photonic crystal cavities. *Optica* **6**, 577–584 (2019).
85. Fiaschi, N. *et al.* Optomechanical quantum teleportation. *Nat. Photonics* **15**, 817–821 (2021).
86. Cui, H. *et al.* Three-dimensional printing of piezoelectric materials with designed anisotropy and directional response. *Nat. Mater.* **18**, 234–241 (2019).
87. Sellers, S. R., Man, W., Sahba, S. & Florescu, M. Local self-uniformity in photonic networks. *Nat. Commun.* **8**, 14439 (2017).
88. Froufe-Pérez, L. S., Engel, M., Sáenz, J. J. & Scheffold, F. Band gap formation and Anderson localization in disordered photonic materials with structural correlations. *Proc. Natl. Acad. Sci.* **114**, 9570–9574 (2017).
89. Diego, M. *et al.* Hypersonic acoustic wave control via hyperuniform phononic nanostructures. Preprint at https://doi.org/10.48550/arXiv.2501.04428 (2025).
90. Oudich, M. *et al.* Photonic analog of bilayer graphene. *Phys. Rev. B* **103**, 214311 (2021).

91. Oudich, M., Deng, Y. & Jing, Y. Twisted pillared phononic crystal plates. *Appl. Phys. Lett.* **120**, 232202 (2022).
92. Burgoyne, H. A., Newman, J. A., Jackson, W. C. & Daraio, C. Guided Impact Mitigation in 2D and 3D Granular Crystals. in *Proceedings of the 2015 Hypervelocity Impact Symposium (HVIS 2015)* vol. 103 52–59 (Elsevier, 2015).
93. Li, F., Anzel, P., Yang, J., Kevrekidis, P. G. & Daraio, C. Granular acoustic switches and logic elements. *Nat. Commun.* **5**, 5311 (2014).
94. Singhal, T., Kim, E., Kim, T.-Y. & Yang, J. Weak bond detection in composites using highly nonlinear solitary waves. *Smart Mater. Struct.* **26**, 055011 (2017).
95. Deng, B., Raney, J. R., Tournat, V. & Bertoldi, K. Elastic Vector Solitons in Soft Architected Materials. *Phys. Rev. Lett.* **118**, 204102 (2017).
96. Deng, B., Wang, P., He, Q., Tournat, V. & Bertoldi, K. Metamaterials with amplitude gaps for elastic solitons. *Nat. Commun.* **9**, 3410 (2018).
97. Kollár, A. J., Fitzpatrick, M. & Houck, A. A. Hyperbolic lattices in circuit quantum electrodynamics. *Nature* **571**, 45–50 (2019).
98. Maciejko, J. & Rayan, S. Hyperbolic band theory. *Sci. Adv.* **7**, eabe9170 (2021).
99. Yu, S., Piao, X. & Park, N. Topological Hyperbolic Lattices. *Phys. Rev. Lett.* **125**, 053901 (2020).
100. Ruzzene, M., Prodan, E. & Prodan, C. Dynamics of elastic hyperbolic lattices. *Extreme Mech. Lett.* **49**, 101491 (2021).
101. Assouar, B. *et al.* Acoustic metasurfaces. *Nat. Rev. Mater.* **3**, 460–472 (2018).
102. Yang, M. & Sheng, P. Sound Absorption Structures: From Porous Media to Acoustic Metamaterials. *Annu. Rev. Mater. Res.* **47**, 83–114 (2017).
103. Li, Y. & Assouar, B. M. Acoustic metasurface-based perfect absorber with deep subwavelength thickness. *Appl. Phys. Lett.* **108**, 063502 (2016).
104. Yang, M., Chen, S., Fu, C. & Sheng, P. Optimal sound-absorbing structures. *Mater. Horiz.* **4**, 673–680 (2017).
105. Peng, X., Ji, J. & Jing, Y. Composite honeycomb metasurface panel for broadband sound absorption. *J. Acoust. Soc. Am.* **144**, EL255–EL261 (2018).
106. Zhu, Y., Donda, K., Fan, S., Cao, L. & Assouar, B. Broadband ultra-thin acoustic metasurface absorber with coiled structure. *Appl. Phys. Express* **12**, 114002 (2019).
107. Ji, J., Li, D., Li, Y. & Jing, Y. Low-Frequency Broadband Acoustic Metasurface Absorbing Panels. *Front. Mech. Eng.* **6**, (2020).
108. Ma, G., Yang, M., Xiao, S., Yang, Z. & Sheng, P. Acoustic metasurface with hybrid resonances. *Nat. Mater.* **13**, 873–878 (2014).
109. Mei, J. *et al.* Dark acoustic metamaterials as super absorbers for low-frequency sound. *Nat. Commun.* **3**, 756 (2012).
110. Cai, X., Guo, Q., Hu, G. & Yang, J. Ultrathin low-frequency sound absorbing panels based on coplanar spiral tubes or coplanar Helmholtz resonators. *Appl. Phys. Lett.* **105**, 121901 (2014).
111. Huang, S. *et al.* Acoustic perfect absorbers via spiral metasurfaces with embedded apertures. *Appl. Phys. Lett.* **113**, 233501 (2018).
112. Wu, Y., Liang, Q., He, J., Feng, J. & Chen, T. Deep-subwavelength broadband sound absorbing metasurface based on the update finger coiling-up method. *Appl. Acoust.* **195**, 108846 (2022).
113. Abrahams, M. P., Oudich, M., Revalor, Y., Vukadinovic, N. & Assouar, B. Hybrid ultrathin metasurface for broadband sound absorption. *Appl. Phys. Lett.* **124**, 151702 (2024).
114. Khan, F. U. & Izhar. State of the art in acoustic energy harvesting. *J. Micromechanics Microengineering* **25**, 023001 (2015).
115. Horowitz, S. B., Sheplak, M., Cattafesta, L. N. & Nishida, T. A MEMS acoustic energy harvester. *J. Micromechanics Microengineering* **16**, S174 (2006).
116. Liu, F. *et al.* Acoustic energy harvesting using an electromechanical Helmholtz resonatora). *J. Acoust. Soc. Am.* **123**, 1983–1990 (2008).
117. Li, B., You, J. H. & Kim, Y.-J. Low frequency acoustic energy harvesting using PZT piezoelectric plates in a straight tube resonator. *Smart Mater. Struct.* **22**, 055013 (2013).
118. Wu, L.-Y., Chen, L.-W. & Liu, C.-M. Acoustic energy harvesting using resonant cavity of a sonic crystal. *Appl. Phys. Lett.* **95**, 013506 (2009).
119. Badreddine Assouar, M. & Oudich, M. Enlargement of a locally resonant sonic band gap by using double-sides stubbed phononic plates. *Appl. Phys. Lett.* **100**, 123506 (2012).

120. Oudich, M., Zhou, X. & Badreddine Assouar, M. General analytical approach for sound transmission loss analysis through a thick metamaterial plate. *J. Appl. Phys.* **116**, 193509 (2014).
121. Assouar, B., Oudich, M. & Zhou, X. Acoustic metamaterials for sound mitigation. *Comptes Rendus Phys.* **17**, 524–532 (2016).
122. Qi, S., Oudich, M., Li, Y. & Assouar, B. Acoustic energy harvesting based on a planar acoustic metamaterial. *Appl. Phys. Lett.* **108**, 263501 (2016).
123. Zhang, Z., Li, Q., Oudich, M., Pan, Y. & Li, Y. Experimental demonstration of enhanced acoustic energy harvesting with a subwavelength metamaterial plate. *New J. Phys.* **22**, 123019 (2020).
124. Oudich, M. & Li, Y. Tunable sub-wavelength acoustic energy harvesting with a metamaterial plate. *J. Phys. Appl. Phys.* **50**, 315104 (2017).
125. Sun, K. *et al.* Self-powered Through-wall communication for dry cask storage monitoring. *Ann. Nucl. Energy* **177**, 109306 (2022).
126. Takahashi, V. L. *et al.* Ultrasonic Power and Data Transfer through Multiple Curved Layers Applied to Pipe Instrumentation. *Sensors* **19**, 4074 (2019).
127. Kaczmarczyk, Z. *et al.* Inductive Power Transfer Subsystem for Integrated Motor Drive. *Energies* **14**, 1412 (2021).
128. Torres, O., Nguyen, T. & Mackenzie, A. *Enabling Wireless Avionics Intra-Communications*. https://ntrs.nasa.gov/citations/20170000686 (2016).
129. Ozeri, S. & Shmilovitz, D. Ultrasonic transcutaneous energy transfer for powering implanted devices. *Ultrasonics* **50**, 556–566 (2010).
130. Covic, G. A. & Boys, J. T. Modern Trends in Inductive Power Transfer for Transportation Applications. *IEEE J. Emerg. Sel. Top. Power Electron.* **1**, 28–41 (2013).
131. Fu, H., Rao, J., Harb, M. S. & Theodossiades, S. Ultrasonic wireless power links for battery-free condition monitoring in metallic enclosures. *Ultrasonics* **114**, 106395 (2021).
132. Kluge, M. *et al.* Wireless Sensing of Physical Parameters Inside Hermetically Enclosed Conductive Envelopes. in 353–359 (American Society of Mechanical Engineers Digital Collection, 2009). doi:10.1115/DETC2007-35481.
133. Kazys, R. & Vaskeliene, V. High Temperature Ultrasonic Transducers: A Review. *Sensors* **21**, 3200 (2021).
134. Ji, J., Heo, H., Zhong, J., Oudich, M. & Jing, Y. Metamaterial-enabled wireless and contactless ultrasonic power transfer and data transmission through a metallic wall. *Phys. Rev. Appl.* **21**, 014059 (2024).
135. Erbe, C. *et al.* The Effects of Ship Noise on Marine Mammals—A Review. *Front. Mar. Sci.* **6**, (2019).
136. Ivansson, S. M. Sound absorption by viscoelastic coatings with periodically distributed cavities. *J. Acoust. Soc. Am.* **119**, 3558 (2006).
137. Leroy, V. *et al.* Superabsorption of acoustic waves with bubble metascreens. *Phys. Rev. B - Condens. Matter Mater. Phys.* **91**, 020301 (2015).
138. Sharma, G. S., Skvortsov, A., MacGillivray, I. & Kessissoglou, N. Acoustic performance of gratings of cylindrical voids in a soft elastic medium with a steel backing. *J. Acoust. Soc. Am.* **141**, 4694 (2017).
139. Meng, H., Wen, J., Zhao, H. & Wen, X. Optimization of locally resonant acoustic metamaterials on underwater sound absorption characteristics. *J. Sound Vib.* **331**, 4406 (2012).
140. Huang, L. Z., Xiao, Y., Wen, J. H., Yang, H. Bin & Wen, X. Sen. Analysis of underwater decoupling properties of a locally resonant acoustic metamaterial coating. *Chin. Phys. B* **25**, 024302 (2016).
141. Shi, K., Jin, G., Liu, R., Ye, T. & Xue, Y. Underwater sound absorption performance of acoustic metamaterials with multilayered locally resonant scatterers. *Results Phys.* **12**, 132 (2019).
142. Dong, H.-W. *et al.* Reflective Metasurfaces with Multiple Elastic Mode Conversions for Broadband Underwater Sound Absorption. *Phys. Rev. Appl.* **17**, 044013 (2022).
143. Dong, H.-W. *et al.* Porous-Solid Metaconverters for Broadband Underwater Sound Absorption and Insulation. *Phys. Rev. Appl.* **19**, 044074 (2023).
144. Khelif, A., Achaoui, Y., Benchabane, S., Laude, V. & Aoubiza, B. Locally resonant surface acoustic wave band gaps in a two-dimensional phononic crystal of pillars on a surface. *Phys. Rev. B* **81**, 214303 (2010).
145. Achaoui, Y., Khelif, A., Benchabane, S., Robert, L. & Laude, V. Experimental observation of locally-resonant and Bragg band gaps for surface guided waves in a phononic crystal of pillars. *Phys. Rev. B* **83**, 104201 (2011).
146. Yudistira, D. *et al.* Nanoscale pillar hypersonic surface phononic crystals. *Phys. Rev. B* **94**, 094304 (2016).
147. Badreddine Assouar, M. & Oudich, M. Dispersion curves of surface acoustic waves in a two-dimensional phononic crystal. *Appl. Phys. Lett.* **99**, 123505 (2011).

148. Länge, K., Rapp, B. E. & Rapp, M. Surface acoustic wave biosensors: a review. *Anal. Bioanal. Chem.* **391**, 1509–1519 (2008).
149. Lim, C., Wang, W., Yang, S. & Lee, K. Development of SAW-based multi-gas sensor for simultaneous detection of CO2 and NO2. *Sens. Actuators B Chem.* **154**, 9–16 (2011).
150. Jin, H. *et al.* Flexible surface acoustic wave resonators built on disposable plastic film for electronics and lab-on-a-chip applications. *Sci. Rep.* **3**, 2140 (2013).
151. Tang, P., Wang, Y., Huo, J. & Lin, X. Love Wave Sensor for Prostate-Specific Membrane Antigen Detection Based on Hydrophilic Molecularly-Imprinted Polymer. *Polymers* **10**, 563 (2018).
152. Topolevsky, R. B. & Redwood, M. A General Perturbation Theory for Elastic Resonators and Its Application to the Monolithic Crystal Filter. *IEEE Trans. Sonics Ultrason.* **22**, 152–161 (1975).
153. Migliori, M., Gabriele, D., Di Sanzo, R., de Cindio, B. & Correra, S. Viscosity of Multicomponent Solutions of Simple and Complex Sugars in Water. *J. Chem. Eng. Data* **52**, 1347–1353 (2007).
154. Fleury, R., Sounas, D., Haberman, M. R. & Alù, A. Nonreciprocal acoustics. *Acoust Today* **11**, 14 (2015).
155. Liang, B., Yuan, B. & Cheng, J. Acoustic Diode: Rectification of Acoustic Energy Flux in One-Dimensional Systems. *Phys. Rev. Lett.* **103**, 104301 (2009).
156. Liang, B., Guo, X. S., Tu, J., Zhang, D. & Cheng, J. C. An acoustic rectifier. *Nat. Mater.* **9**, 989–992 (2010).
157. Li, X.-F. *et al.* Tunable Unidirectional Sound Propagation through a Sonic-Crystal-Based Acoustic Diode. *Phys. Rev. Lett.* **106**, 084301 (2011).
158. Wang, X.-P., Wan, L.-L., Chen, T.-N., Liang, Q.-X. & Song, A.-L. Broadband acoustic diode by using two structured impedance-matched acoustic metasurfaces. *Appl. Phys. Lett.* **109**, 044102 (2016).
159. Oliner, A. & Hessel, A. Guided waves on sinusoidally-modulated reactance surfaces. *IRE Trans. Antennas Propag.* **7**, 201–208 (1959).
160. Cassedy, E. S. & Oliner, A. A. Dispersion relations in time-space periodic media: Part I—Stable interactions. *Proc. IEEE* **51**, 1342–1359 (1963).
161. Taravati, S. Self-biased broadband magnet-free linear isolator based on one-way space-time coherency. *Phys. Rev. B* **96**, 235150 (2017).
162. Taravati, S. Aperiodic space-time modulation for pure frequency mixing. *Phys. Rev. B* **97**, 115131 (2018).
163. Taravati, S. Giant Linear Nonreciprocity, Zero Reflection, and Zero Band Gap in Equilibrated Space-Time-Varying Media. *Phys. Rev. Appl.* **9**, 064012 (2018).
164. Taravati, S. & Eleftheriades, G. V. Pure and Linear Frequency-Conversion Temporal Metasurface. *Phys. Rev. Appl.* **15**, 064011 (2021).
165. Fleury, R., Sounas, D. L. & Alù, A. Subwavelength ultrasonic circulator based on spatiotemporal modulation. *Phys. Rev. B* **91**, 174306 (2015).
166. Shen, C., Zhu, X., Li, J. & Cummer, S. A. Nonreciprocal acoustic transmission in space-time modulated coupled resonators. *Phys. Rev. B* **100**, 054302 (2019).
167. Zhu, X. *et al.* Non-reciprocal acoustic transmission via space-time modulated membranes. *Appl. Phys. Lett.* **116**, 034101 (2020).
168. Oudich, M., Deng, Y., Tao, M. & Jing, Y. Space-time phononic crystals with anomalous topological edge states. *Phys. Rev. Res.* **1**, 033069 (2019).
169. Trainiti, G. & Ruzzene, M. Non-reciprocal elastic wave propagation in spatiotemporal periodic structures. *New J. Phys.* **18**, 083047 (2016).
170. Wang, Y. *et al.* Observation of Nonreciprocal Wave Propagation in a Dynamic Phononic Lattice. *Phys. Rev. Lett.* **121**, 194301 (2018).
171. Trainiti, G. *et al.* Time-Periodic Stiffness Modulation in Elastic Metamaterials for Selective Wave Filtering: Theory and Experiment. *Phys. Rev. Lett.* **122**, 124301 (2019).
172. Sugino, C., Ruzzene, M. & Erturk, A. Nonreciprocal piezoelectric metamaterial framework and circuit strategies. *Phys. Rev. B* **102**, 014304 (2020).
173. Chen, Z. *et al.* A tunable acoustic metamaterial with double-negativity driven by electromagnets. *Sci. Rep.* **6**, 30254 (2016).
174. Wan, S., Cao, L., Zhu, Y., Oudich, M. & Assouar, B. Nonreciprocal Sound Propagation via Cascaded Time-Modulated Slab Resonators. *Phys. Rev. Appl.* **16**, 064061 (2021).
175. Wan, S. *et al.* Low-frequency nonreciprocal flexural wave propagation via compact cascaded time-modulated resonators. *Appl. Phys. Lett.* **120**, 231701 (2022).